Journal of Hydrology 531 (2015) 475–493

Contents lists available at ScienceDirect

Journal of Hydrology

journal homepage: www.elsevier.com/locate/jhydrol

Landform controls on low level moisture convergence and the diurnal cycle of warm season orographic rainfall in the Southern Appalachians

Anna M. Wilson, Ana P. Barros *

Civil and Environmental Engineering Department, Pratt School of Engineering, Duke University, Durham, NC 27708, United States

ARTICLE INFO

Article history:
Available online 11 November 2015

Keywords:
Complex terrain
Numerical weather simulations
Precipitation microphysics
Orographic enhancement
Seeder-feeder mechanism

SUMMARY

The Advanced Weather Research and Forecasting (WRF) model was used to simulate two warm season events representative of reverse orographic enhancement of warm season precipitation in the Southern Appalachians under weak (9–12 July, 2012) and strong (12–16 May, 2014) synoptic forcing conditions. Reverse orographic enhancement refers to significant enhancement of rainfall intensity (up to one order of magnitude) at low elevations in the inner mountain valleys, but not in the ridges. This is manifest in significant increases of radar reflectivity observations and associated integral quantities (rain rate) at low levels (within 500 m of the surface), as well as changes in the observed microphysical properties of rainfall (raindrop size distribution). Analysis of high-resolution (1.25 km × 1.25 km) WRF simulations shows that the model captures the march of observed rainfall, though not the timing in the case of strong synoptic forcing. For each event, the results show that the space–time variability of rainfall in the inner region is strongly coupled to the development and persistence of organized within-valley low-level moisture convergence that is a necessary precursor to valley fog and low level cloud formation. Microphysical interactions among precipitation from propagating storm systems, and local low-level clouds and fog promote coalescence efficiency through the seeder-feeder mechanism leading to significant enhancement of rainfall intensity near the ground as shown by Wilson and Barros (2014). The simulations support the hypothesis that ridge–valley precipitation gradients, and in particular the reverse orographic enhancement effects in inner mountain valleys, are linked to horizontal heterogeneity in the vertical structure of low level clouds and precipitation promoted through landform controls on moisture convergence.

© 2015 Elsevier B.V. All rights reserved.

1. Introduction

The hydrometeorology of the Southern Appalachian Mountains (SAM), which are characterized by moderate topography and complex landforms with wide cross-valleys and nested systems of ridges and valleys in the inner region, is typical of middle mountains (defined as mid-sized mountains with altitudes between 500 and 2000 m) in humid climates. Light rainfall and fog play an important role in the water budget of the Southern Appalachians. Light rainfall in particular has been shown to contribute significantly to the total precipitation depending on characteristics such as season, year, and rain rate threshold, through in situ measurements taken since 2007 in the Pigeon River Basin (see map in Fig. 1; Prat and Barros, 2010; Wilson and Barros, 2014; Fig. 2 in this paper). In terms of fog, Wilson and Barros (2014) used a stochastic raindrop population dynamics model and showed that fog and low level clouds in this region act as a significant modifier to the classical notion of orographic enhancement of rainfall with elevation through the seeder-feeder interactions that explain higher rainfall rates at low elevations in the inner mountain valleys, and specifically early morning and daytime valley rainfall maxima. The seeder-feeder process, first proposed by Bergeron (1950, 1965, 1968) and further described by Cunningham (1951) among others (for a comprehensive review see Barros and Lettenmaier, 1994), describes a mechanism by which higher level clouds precipitate and provide "seed" for the lower level orographic clouds, which act as the "feeder" and, through their additional moisture and droplet concentration interacting with the falling rain droplets, result in precipitation enhancement. This work aims to examine lower-tropospheric moisture convergence under different synoptic conditions to investigate whether it is sufficient to support low level cloud formation consistent with the reverse orographic enhancement mechanisms seen in Wilson and Barros (2014).

* Corresponding author at: Duke University, Box 90287, Room 121 Hudson Hall, Durham, NC 27708-0287, United States.
E-mail address: barros@duke.edu (A.P. Barros).

http://dx.doi.org/10.1016/j.jhydrol.2015.10.068
0022-1694/© 2015 Elsevier B.V. All rights reserved.

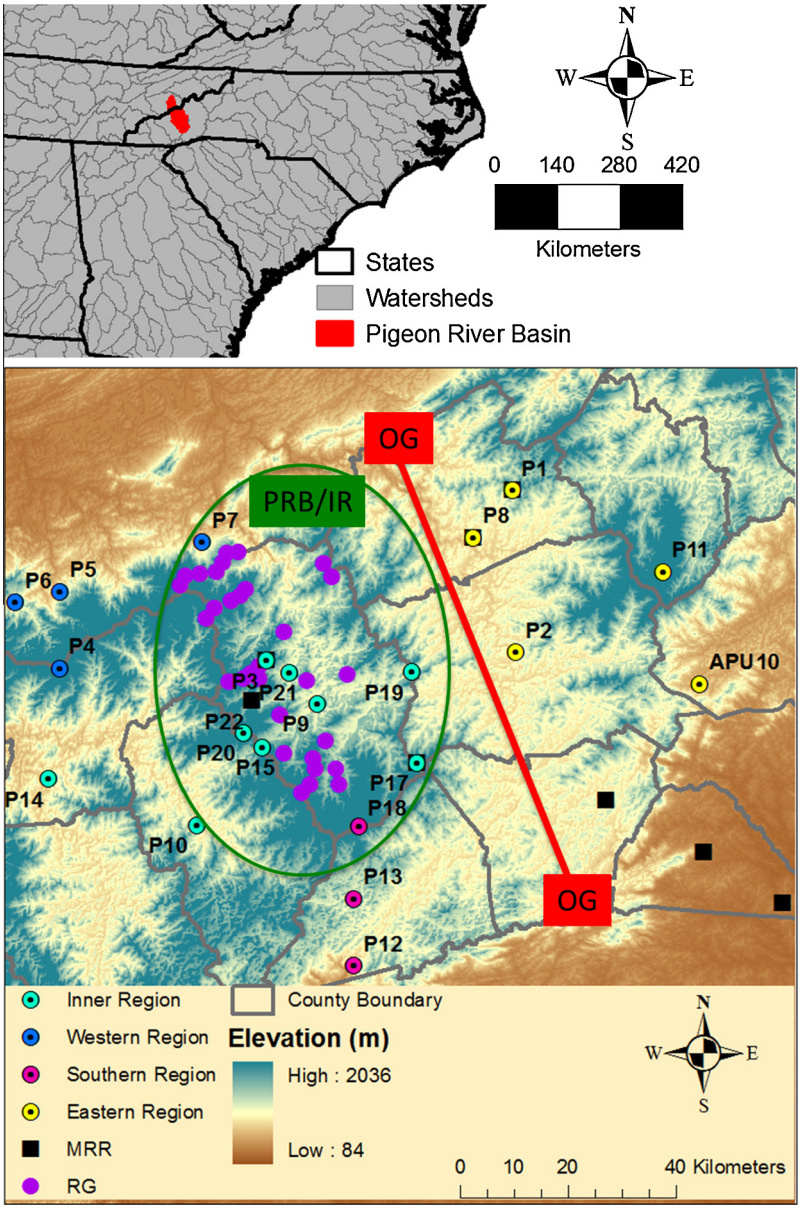


Fig. 1. (Top) Map of the study region shown in context of the southeastern United States; (bottom) instrument (MRR, PARSIVEL) locations during the period 2011–2014, along with the rain gauge network in the Pigeon River Basin (Haywood County). The area in the bottom map is shown in red in the top map. The Pigeon River Basin corresponds with the inner region and is labeled PRB/IR inside a green circle. The open gap (OG region) is labeled with a red line. (For interpretation of the references to color in this figure legend, the reader is referred to the web version of this article.)

For this purpose, the WRF model is used to simulate two multi-day events for weak (July 9–12 2012) and strong (May12–16, 2014) synoptic forcing. The underlying hypothesis is that persistent low level convergence patterns are required locally for the development of the layered heterogeneous vertical structure of condensate and hydrometeors required by the seeder-feeder mechanism, and that the spatial variability of precipitation in regions of complex terrain, and in particular the reverse orographic enhancement effect in inner mountain valleys, can be explained by the space–time patterns of moisture convergence that result from the modification of the prevailing synoptic circulations by the terrain. The numerical model will function as a virtual laboratory toward improving our understanding of the physics in moist atmospheric processes in the SAM that should be transferable elsewhere.

Cloud immersion is an important water source for Southern Appalachian ecosystems (Berry et al., 2014; Culatta and Horton, 2014; among others). One of the potential global consequences of climate change is the raising of cloud base/reduction of low cloud over land (Anderson et al., 2011). For instance, more than a decade ago, loss of forest species was already being attributed to an observed reduction in low level cloudiness in Costa Rica (Foster, 2001; Pounds et al., 1999), and urbanization has recently been shown to cause a decrease in fog frequency and an increase in cloud ceilings in California (Williams et al., 2015). Some studies suggest that cloud base height is already increasing in the SAM (e.g. Sun et al., 2007), but this is uncertain (Richardson et al., 2003). Therefore, any potential increases in cloud base height or decreased fog presence, whether caused by climate change related drying or by the growing population of the southeast US (Terando et al., 2014; US Census Briefs, 2011), present a threat to regional biodiversity and ecosystem sustainability. This is a critical part of the motivation to understand important processes helping to regulate vulnerable ecosystems. Specifically, it is important to

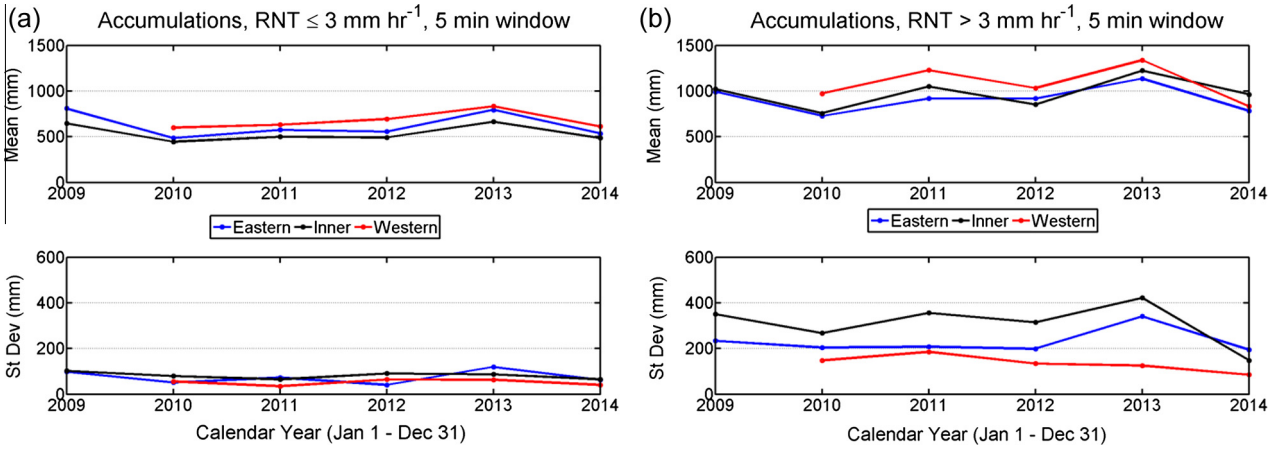


Fig. 2. Average rainfall totals and standard deviations from the long term tipping bucket rain gauge network for six calendar years from 2009 to 2014 are presented for different ridgelines and valleys in the Pigeon River Basin, separated by an intensity threshold of 3 mm h^{-1}.

quantify and fully understand the diurnal cycle of freshwater input and consequently the water budget, as well as the diurnal cycle of low level clouds that in turn strongly affects the diurnal cycle of radiative forcing. Another implication of explaining the reverse orographic effect in the inner mountain region is to improve predictability of localized heavy rainfall that results in risks to life and property through hazards such as landslides, debris falls, or flash flooding (e.g., Wooten et al., 2008; Tao and Barros, 2013, 2014).

The manuscript is organized as follows. Analysis of the observations, including a description of the instrumentation used in this study, will be presented in Section 2. Section 3 reviews previous like-minded modeling work conducted using WRF as a preamble to presenting the specific WRF model configuration and grid setup used for this study, including sensitivity studies conducted to select a suitable microphysical parameterization for this work. In Section 4, detailed analysis of the model simulations for the two events are presented. Conclusions, discussion, and future work will be discussed in Section 5.

2. Observations

2.1. Instrument description

The instruments that have been used to measure low level moisture and rainfall in situ at high elevations and to conduct studies throughout ridges and valleys in the region include: tipping bucket rain gauges, at resolutions ranging from 0.1 mm to 1.0 mm; METEK Micro Rain Radars (MRRs), at range gate resolutions ranging from 35 m to 150 m; fog collectors; and PARSIVEL optical disdrometers. Data from other instruments, including microwave radiometers and 2-dimensional video disdrometers, are also available during selected time periods but those listed in the previous sentence are the sensors on which this paper will focus. The rain gauges and disdrometers record many of the characteristics of a precipitation event at the ground, from the microphysical scale to the rainfall depth, the fog collectors provide information about the horizontal advection of cloud water and presence of stationary fog, and the MRRs provide information on the vertical structure of the event. A brief description of each of the instruments follows.

The rain gauges use a tipping bucket mechanism in order to measure rainfall accumulations. Each time the bucket tips, the datalogger records a date/time stamp down to the second. Limitations with this instrument include the time drift in the dataloggers making the time stamp inexact, and the documented difficulty of tipping bucket rain gauges at very high rain rates (it is not possible to measure the rain during the time the bucket mechanically takes to tip), in very low rain rates (where there might be accumulation beneath the instrument's resolution, and where the date/time stamp might not be helpful in terms of when the rain was falling (over what duration)), and in windy conditions (Sevruk and Nespor, 1998; Mekonnen et al., 2014 for one recent example).

The MRRs operate at 24 GHz (*K*-band) using the frequency modulated continuous wave principle. The fall velocity of hydrometeors leads to a Doppler shift in the received frequency in addition to the range frequency shift. The fall velocity is the first moment of the Doppler spectra. The DSD is determined using the relationship between spectral reflectivity and single particle backscattering cross section (METEK, 2012). A key limitation in this retrieval is that it does not account for wind (horizontal or vertical) at any scale. Other limits result from the sampling volume (profile only) and measurement resolution (gate depth).

Detailed description of the fog collectors, manufactured by Professor James Juvik of the University of Hawaii, can be found in a Comment by Juvik and Nullet (1995, Section 2). Briefly, louvered cylinders collect lateral moisture from fog and then the water drips through a funnel and a vinyl tube into a covered tipping bucket rain gauge. There is an inverted cone over the top of the cylinder to block vertical rain from entering the gauge. Limitations to this sensor are similar to those discussed for the rain gauges, in particular the uncertainty in the timing of the actual fog water collection as represented by the tips of the bucket.

The PARSIVEL disdrometer uses a laser beam between the two heads of the instrument to measure particles. When precipitation particles pass through the laser beam, the portion of the beam that is blocked is used to measure the diameter of the particle. Velocity is determined using the duration of the blocking of the beam. The PARSIVEL disdrometer can reliably measure liquid particles with diameter between 0.25 and 5 mm. The PARSIVEL disdrometers have been shown to have limitations on the measurement of very small particles and under windy conditions (Angulo-Martínez and Barros, 2015; Tokay et al., 2014), although the more recent PARSIVEL2 is an improvement most notably in this respect.

2.2. Observations and analysis

General observations taken during an intensive observing period during 2014 will be analyzed here in order to provide a

sense of the diurnal cycle of fog and rain in the warm season, as well as an overall characterization of the microphysical and vertical structure of the atmosphere in this region. Observations specific to the case studies will be discussed in rigorous detail in Section 4.

MRRs were located along altitudinal gradients in the inner mountain region, in the open gap of the French-Broad river valley, and on the southeastern slopes (see map in Fig. 1). The longest observation periods are available for the first two regions.

The PARSIVEL disdrometers were located in a dense array during 2014 with selected observations available for certain locations in the inner region and open gap before that (e.g. 2008–2013). Previous work (Prat and Barros, 2010; Angulo-Martínez and Barros, 2015; Wilson and Barros, 2014) reported on the latter. Here, we focus on 2014 observations during the Integrated Precipitation and Hydrology Experiment (IPHEx, Barros et al., 2014). PARSIVELs model 1 and model 2 were used. Some were paired so that we could assess the differences between the two instruments. The disdrometers were always paired with tipping bucket rain gauges. The important point about their differences is that under similar operating conditions PARSIVEL1 generally underestimates the number of very small drops compared to PARSIVEL2 (Angulo-Martínez and Barros, 2015). Both PARSIVEL1 and 2 may overestimate midsized drops. These limitations are important to keep in mind when considering the microphysical parameters such as mass weighted mean diameter and standard deviation computed from these observations.

To illustrate the inter-annual variability of the water input to this region at the watershed scale, the average rain gauge totals for five different calendar years are presented in Fig. 2, separated by intensity (3 mm h^{-1}, using a 5 min window surrounding each tip to compute the rain intensity). Basic statistics were calculated for different regions in the SAM (Fig. 1): the western ridges of the Pigeon River Basin, the inner mountain region, and the seven gauges in the southeastern part of the watershed. The averages and standard deviations for gauges located in each area were plotted and show spatial variability among ridgelines with the precipitation amounts increasing from the southeast to the northwest. As mentioned in Section 1, the contribution of light rainfall to the yearly precipitation total can be up to 40% (see 2009 and 2010 in particular), with percentages reaching 60% regularly during certain seasons and higher (80–90% in the fall and winter season) during dry years. Intra-ridge variability is also much higher in the heavier rainfall amounts than in the light. For the heavier rainfall, within ridge variability is the highest in the inner mountain region, where the landform is most complex.

In Fig. 3a, data taken by two fog collectors deployed on a western ridge (P4) and in the inner region (P3) during June, July, and August 2014 are presented. Occurrence frequency is calculated to reveal the diurnal cycle, and can be represented as follows for each respective gauge at P3 and P4, where b is the number of tips:

$$Freq = \frac{\bar{b}_{4hrperiod}}{\bar{b}_{daily}} \quad (1)$$

The data reveal clear morning fog and afternoon rain peaks for the P3 location in the inner mountain region. At P4, which is a location frequently inside the cloud deck, there is an overnight/early morning fog peak. The rain frequency curve does not show an afternoon rain peak as in P3, although the magnitude is not high, the rain peak is also in the overnight hours (0–4 local). At P4, the contribution of fog water is very high, in fact on the same order of magnitude as the rain reported by the rain gauges at that location (Fig. 3b). At this location during this study, throughfall was not considered – only horizontal capture and vertical rainfall measured at an open site collocated with existing National Park Service air quality and meteorological instrumentation.

To assess microphysical characteristics, mass spectrum parameters of the drop size distribution observed by the optical disdrometers were calculated. The disdrometers recorded observations at 10 s intervals throughout their deployment. In Fig. 4, the diurnal cycle of mass weighted mean diameter and its standard deviation are presented for selected altitudinal gradients (P3, P9 and P22 during June 2014; P9 and P22 are valley locations). The two valley

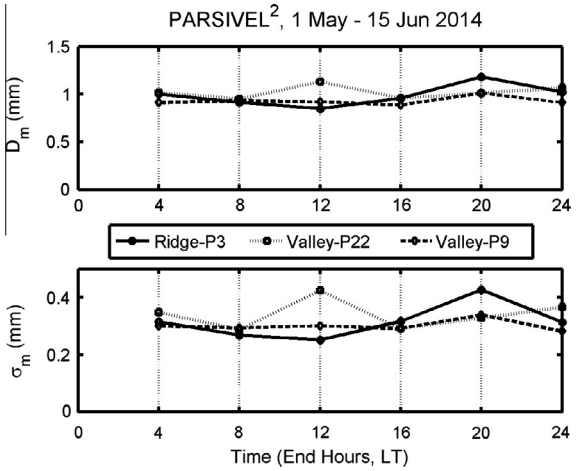


Fig. 4. The average diurnal cycle of mass weighted mean diameter and its standard deviation are presented here along one altitudinal gradient (P3 and P9, P22 in Fig. 1). There were approximately ~9000 samples of each D_m and σ_m pair.

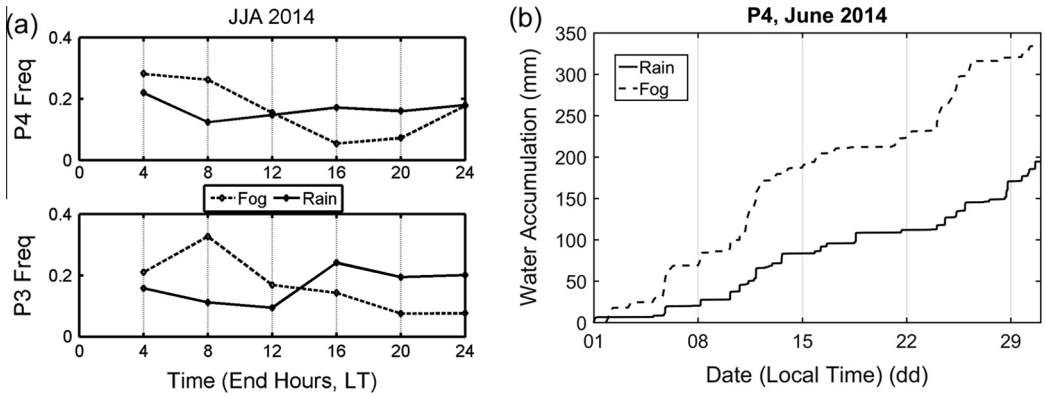


Fig. 3. (a) Fog and rain diurnal cycles are presented based on frequency of occurrence for two different locations Purchase Knob (P3 in Fig. 1) in the inner mountain region and Clingman's Dome (P4 in Fig. 1) on the western ridges. (b) Accumulations from the fog collector and the rain gauge are presented for June 2014 at P4.

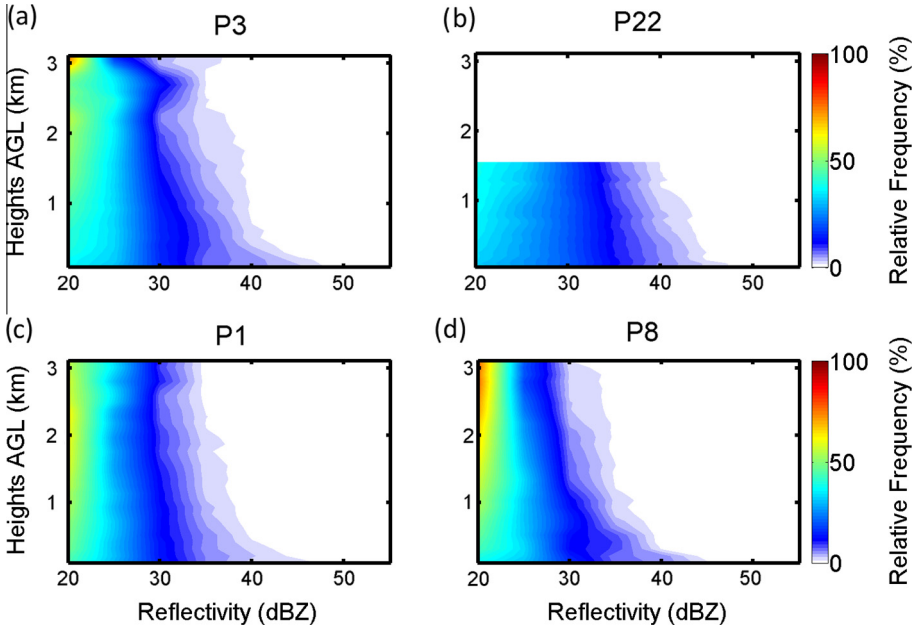


Fig. 5. Contoured frequency with altitude diagrams (CFADs) are presented for Micro Rain Radars making observations along altitudinal gradients in the inner region (top row, L to R – P3 and P22) and open gap (bottom row, L to R – P1 and P8). These provide information on the vertical profile of hydrometeors during rain events recorded by collocated instruments. The titles correspond to the locations in Fig. 1. CFADs are presented here for all observed reflectivity values over 20 dBZ.

locations are different in that low clouds were observed more frequently than fog at P22, whereas fog was a common occurrence at P9. Still, there are clear differences in the diurnal cycle of both the mass weighted mean diameter and its standard deviation. The mass weighted mean diameter is computed as follows:

$$D_m = \frac{\int_0^\infty N(D)D^3 DdD}{\int_0^\infty N(D)D^3 dD} \quad (2)$$

These parameters are a useful characterization of the drop size distribution because they provide information on how the liquid water content is distributed through the number concentration. Fig. 4 shows a shift in the peak mass weighted mean diameter value from the valley at P22 in the morning, to the afternoon at P3. At P9, the diameter stays relatively constant throughout the day, although it follows the pattern of P3 more closely than P22, perhaps relating to the more frequent fog presence observed there. The standard deviation follows the same pattern, showing that as the mass of the drop size distribution increases or decreases, so does the breadth. These variables follow a power law relationship with each other (Williams et al., 2014).

Last, the MRRs provide observations of the vertical profiles of reflectivity as a function of time. The radars record observations every 10 s. Analysis was done using 1 min averaged data. The MRR profiles are presented using a version of contoured frequency with altitude (CFAD) diagrams (Yuter and Houze, 1995), where all incidences of reflectivity values over a threshold (20 dBZ in this case) are included. When there are values at that gate over the minimum threshold, their frequency of occurrence at each gate is plotted. Contours are shown for every 1% change. In Fig. 5, CFADs are shown for four MRRs making observations along altitudinal gradients in the inner region and open gap. These provide information on the vertical profile during rain events recorded by collocated instruments. While the increase in reflectivity values at near-surface range gates on the MRR is often attributed to attenuation, previous work has shown that in this region the lower range gates (within 300 m of ground level) correspond best with rain rates observed by independent collocated instruments (rain gauges and disdrometers) (Wilson and Barros, 2014).

In the CFADs presented here of observations taken during IPHEx (May–June 2014), note that P22, the valley location in the inner region, was set up at a higher vertical resolution, with one gate every 50 m beginning at 50 m above ground level (AGL), whereas the other sensors are spaced every 100 m beginning at 100 m AGL. Two major differences are illuminated in the plots between the open gap ridge and valley observations (P1 and P8 respectively). First, there is a higher frequency of low level reflectivity greater than 40 dBZ in the open gap valley location (P8) than in the open gap ridge location (P1). Second, the valley location also shows a "nose" of higher frequencies in the low level gates between 30 and 40 dBZ. P3, the inner region ridge location, shows similar behavior to that found in previous work (Wilson and Barros, 2014) with a sharp decrease just above 2 km AGL (the "active depth" of the atmosphere in the inner region), and a steep increase at the lowest levels. At P22, the reflectivity gradient is less steep than the corresponding ridge. These observations are consistent with the frequent light rainfall measured in the inner mountain region, and the vertical gradient indicates low level enhancement of rainfall through the seeder-feeder mechanism when synoptic or meso-scale cyclones pass by. This difference in characteristics along the altitudinal gradients is a function of the very different surrounding terrain of these two areas, with P3 and P22 in an area of highly complex terrain and nested valleys, and P8 and P1 in the open gap, configured within the French Broad river valley in such a way to not be affected so strongly by blocking particularly when winds are northwesterly.

The microphysics, diurnal cycle, variability, and vertical structure of low level enhancement in the Southern Appalachians, using observations made over an extended observing period during 2014 and a long term high density tipping bucket rain gauge network show the same signature seen during the 2012 Intensive Observing Period (IOP; Wilson and Barros, 2014). The enhancement of rainfall through the input of low level moisture in this region is an important contribution to the water budget overall, due to its effect on precipitation events documented by Wilson and Barros (2014),

and as seen in particular in the vertical structure profiles. We hypothesize that low level moisture convergence into the inner region is necessary to form the fog banks and low level clouds that augment synoptic scale rainfall, indicating that the space–time hot-spots of moisture convergence should directly correlate with areas experiencing reverse orographic enhancement. Furthermore, it is expected that these areas of persistent convergence will be modulated strongly by the terrain, and therefore will vary from event to event depending on the wind modification by topography.

3. WRF model description and setup

3.1. Previous research

Previous work has shown that processes active within 2 km of ground level can have profound impacts on rain intensities and accumulations at the surface. Wilson and Barros (2014) used an explicit raindrop population dynamics column model (Prat and Barros, 2007), which simulates drop–drop interactions in the liquid phase, to illustrate and explain the importance of seeder-feeder interactions between synoptic rainfall and localized low level moisture. Enhanced coalescence is the key pathway that can explain observed DSDs as well as the rainfall rates measured by collocated RGs and disdrometers. In addition, MRR observations of the vertical profile of radar reflectivity show changes when low level enhancement is present. Specifically, during rainfall events with/without significant low level influence, the surface rain rate correlates best with reflectivity at 600 m/150 and 300 m above the surface (Prat and Barros, 2010; Wilson and Barros, 2014).

Those results prompted this study to investigate differences in moisture convergence patterns that are necessary to support fog and low-level cloud formation under distinct synoptic forcing. For this purpose, we make use of the Advanced Research version of the Weather Research and Forecasting Model (WRF) Version 3.5.1 to simulate one of the 2012 multi-day events from previous work (9–12 July) with well documented low level enhancement of rainfall under weak synoptic forcing in the French-Broad River valley (cross-mountain open gap region), as well as a 2014 storm (14–15 May, simulation conducted from 12 to 16 May) that occurred during the IPHEx IOP and corresponded to strong synoptic forcing. Daily weather maps created by the National Center for Environmental Prediction Weather Prediction Center (www.wpc.ncep.noaa.gov/dailywxmap) are provided for each of the cases in Figs. 6 (Case 1) and 7 (Case 2) to indicate the frontal locations and pressure variations over the region during the simulations.

Not surprisingly, many studies have detailed the importance of wind fields in cases of orographic modification of precipitation processes (e.g. Kunz, 2011; Yuter et al., 2011; Smith et al., 2009). WRF does have documented issues with producing accurate near surface wind speed fields particularly in areas of complex terrain, with overestimation in valleys and underestimation at ridges (Jiménez and Dudhia, 2012). Hanna and Yang (2001) list various sources of near surface wind errors in the lower atmosphere, including the fact that random turbulent processes are not appropriately represented in the models, errors exist in subgrid terrain/land use, and the underestimation of vertical temperature gradients in the lowest 100 m overnight can make the boundary layer less stable than observed. In addition, compensating for this effect with more vertical levels does not necessarily correct the problem for specific variables, primarily because of the necessarily coarse terrain representation in WRF, although boundary layer mesoscale structures can improve with increased vertical resolution (e.g. Zhang et al., 2013), and horizontal resolution too, particularly in regions of complex terrain and in terms of realistic structures if not timing (Mass et al., 2002).

In the context of fog forecasting, van der Velde et al. (2010) found that high vertical resolution is required for modeling fog formation and growth, and for the maintenance of lifted fog after it

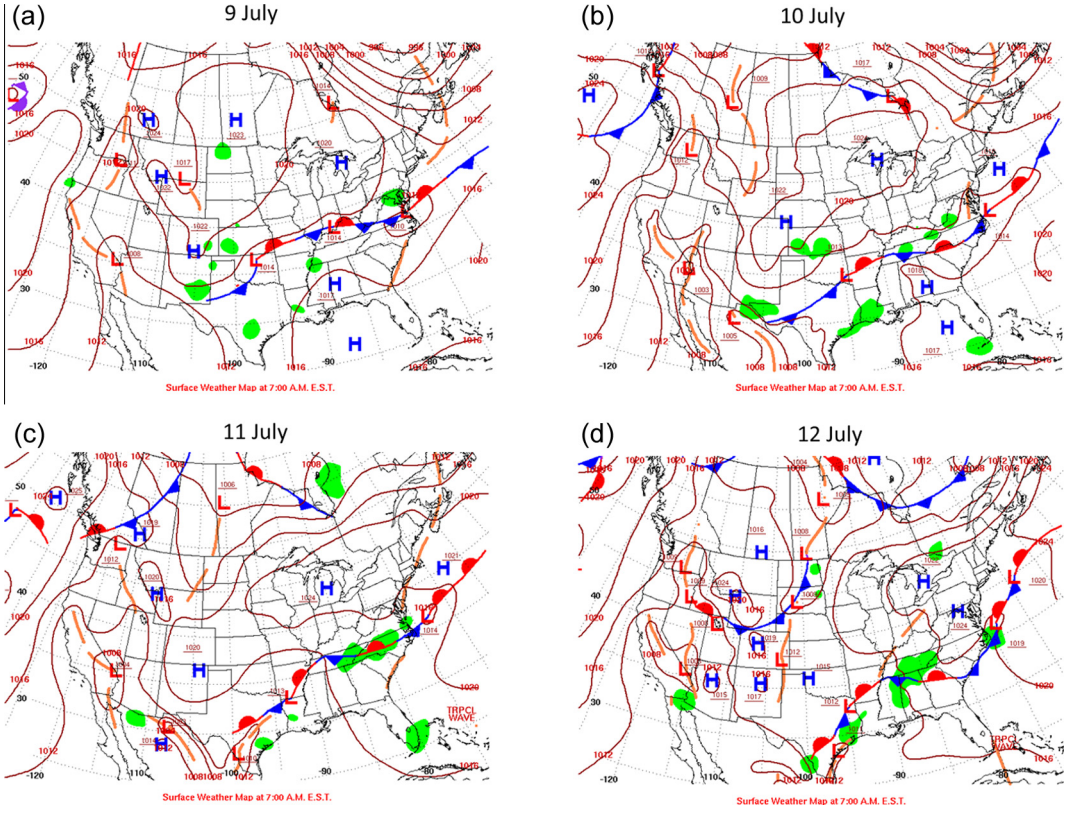


Fig. 6. Daily weather maps for the July 2012 case are presented to help describe the synoptic situation.

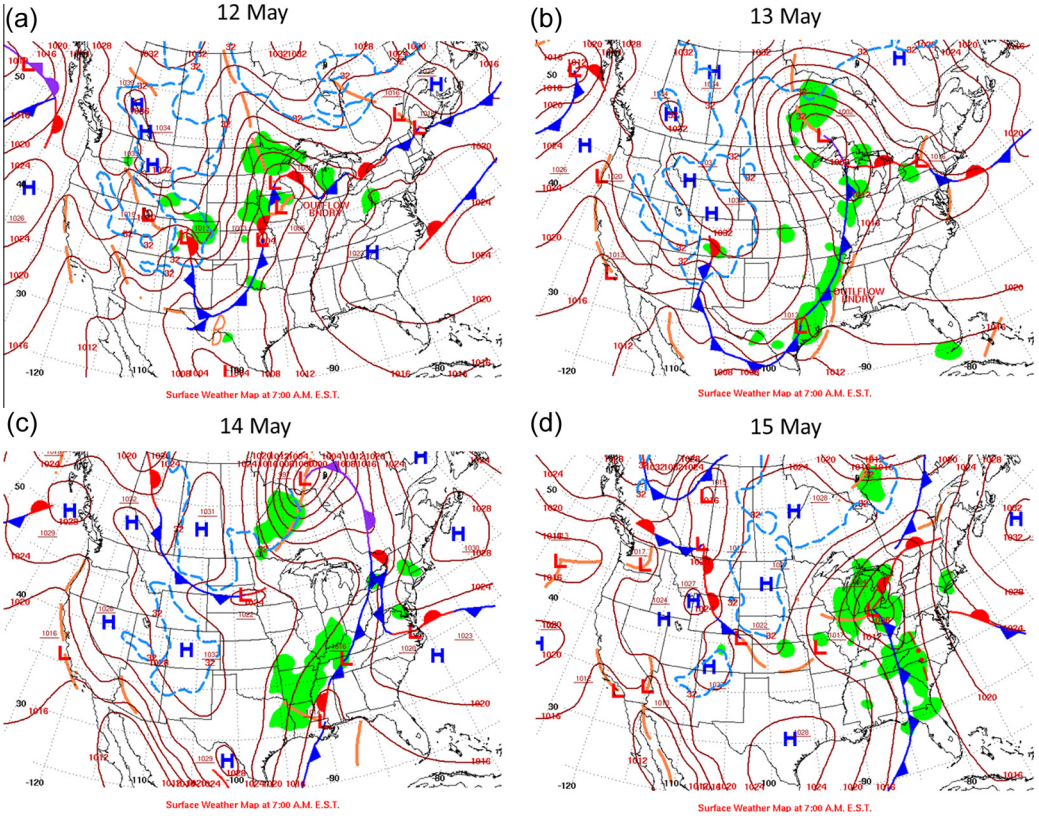


Fig. 7. Daily weather maps for the May 2014 case are presented.

becomes a low level stratus deck. Small scale details in wind fields and turbulence parameterization are highly important in these processes. Hu et al. (2014) assessed WRF's ability to forecast advection fog and found more sensitivity to initial conditions of potential temperature and horizontal wind components than moisture related variables such as mixing ratio. This led to the conclusion that turbulent mixing and moisture advection are major factors contributing to formation of fog, at least in their case study of an event in February 2007 in North China. In addition, the orographic seeder-feeder mechanism has been studied with the WRF model before; Viale et al. (2013) found that in the Andes, orographically enhanced rainband updrafts associated with cold fronts interacting with orographically enhanced midlevel stratiform clouds caused larger precipitation rates upstream. When the simulation was run with the Andes' peaks at lower elevations, they found that the extreme height of the Andes was necessary in this situation to cause stronger lifting, slower movement, and generate the vertical structure necessary to enhance rainfall.

In this study, we use the standard WRF terrain representation at 30 arc-sec that matches closely with the grid resolution that we are using – however, as described in Section 5, in future work the terrain representation will be modified, i.e. we will upscale higher resolution terrain (we will conduct testing using standard WRF methods as well as fractal upscaling as in Bindlish and Barros (1996)) to preserve the topographic complexity at higher spatial resolution.

3.2. WRF model setup

The simulation was conducted on the Yellowstone system (Computational and Information Systems Laboratory, 2012) using Advanced Research WRF Version 3.5.1 (Skamarock et al., 2008), and we rely on previous experience from WRF simulations of Tropical Storm Ivan in the SAM for selecting physical parameterization as well as to specify initial and boundary conditions (Sun and Barros, 2012, 2013). WRF solves the three-dimensional, fully compressible, non-hydrostatic Euler equations, using terrain following (eta) vertical coordinates and Arakawa C-grid staggering in the horizontal. The physical parameterizations used for the simulations are: Milbrandt and Yau (2005a,b) double moment microphysics, the Kain–Fritsch cumulus parameterization scheme in the first two domains (Kain, 2004), the Rapid Radiative Transfer Model (RRTM) longwave radiation scheme (Mlawer et al., 1997), the simple cloud interactive short wave radiation scheme (Dudhia, 1989), the unified Noah land-surface model (Tewari et al., 2004), the Mellor–Yamada–Janjic (MYJ) planetary boundary layer scheme (Janjic, 1994), and the Eta similarity theory surface layer scheme (Janjic, 1994). Initial and boundary conditions are specified using the National Centers for Environmental Prediction (NCEP) Final Operational Global Analysis (FNL; Kalnay et al., 1996). Briefly, these data are produced every six hours on $1^\circ \times 1^\circ$ grids from the Global Data Assimilation System (GDAS). Data are available at 27 levels including the surface. Available forcing datasets have a variety of different strengths and weaknesses, and going to higher resolution is not always advised. We have chosen this forcing dataset based on the testing reported in Sun and Barros (2012), where NCEP FNL was reported to capture storm structure and evolution in this region more accurately than North American Regional Reanalysis (NARR), even though NARR is at higher resolution.

The numerical domain (Fig. 8) consists of three one-way nests defined on a Lambert conformal projection. The first two nests are at a 1:3 grid resolution ratio and the second and third are at a 1:4 resolution ratio. The grids are at resolutions of 15, 5, and 1.25 km. The horizontal grid sizes used in the 3 nests are

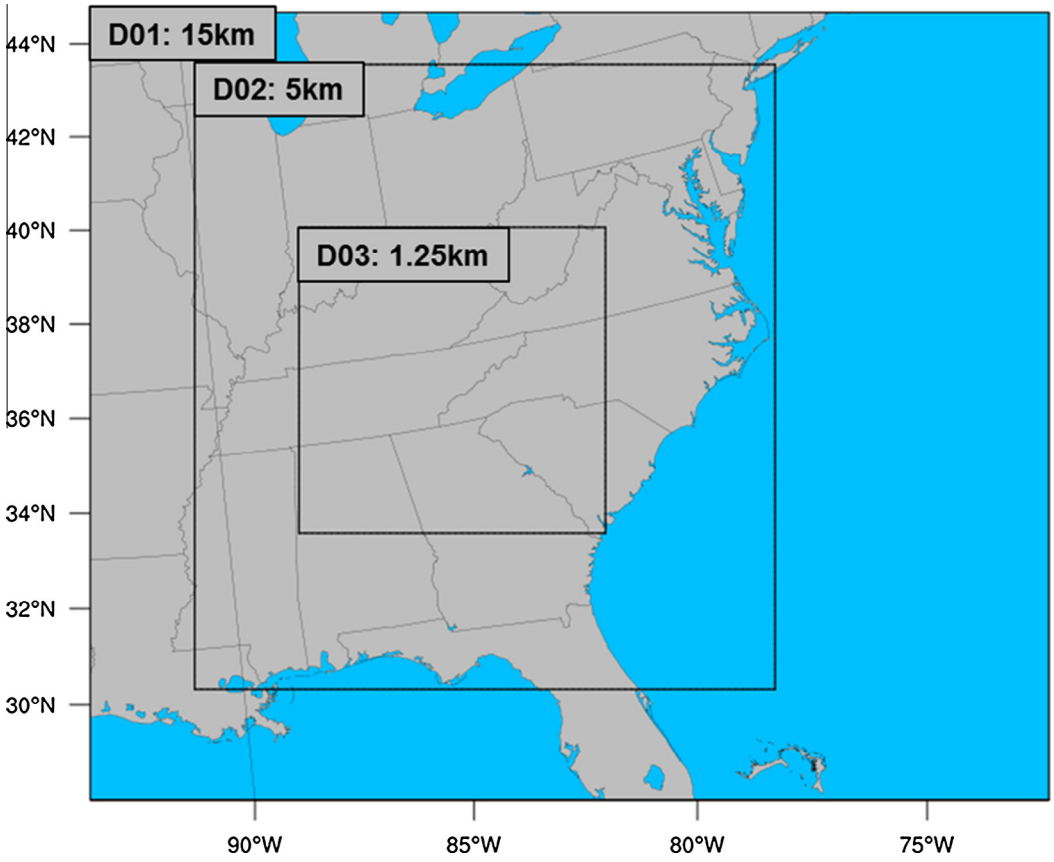


Fig. 8. The three one-way nested WRF domains are shown here, at 15–5–1.25 km resolution respectively.

147 × 121, 267 × 288, and 552 × 552, with 60 vertical grid levels, 4 soil layers and model top at 50 h Pa. The numerical domain was designed after Sun and Barros (2012, 2013) to minimize the effect of the steepness of the terrain, and to minimize the potential damping by lateral boundary conditions. Based on simulations conducted over the Andes in Sun and Barros (2015), we also run the model with 60 vertical grid levels instead of 50 in order to be able to resolve the vertical structure in particular at the lower levels, within the relevant first 2 km above ground level as discussed earlier. Other tests were conducted with the 50 standard levels and then by doubling the standard levels (both including seven layers in the lowest kilometer). Finally, 60 levels with a higher density in the lowest kilometer were used. Instead of 7, there are 14 layers in the lowest 1 km above the ground in our scheme. The goal of this study is to focus on processes occurring in the near surface, so it is necessary to have this part of the atmosphere well represented in the model. Model spin-up is done for 6 h for each case.

Based on previous work (e.g. Erlingis and Barros, 2014), the MYJ, a local PBL (Planetary Boundary Layer) parameterization was selected with the objective of better capturing the spatial heterogeneity of low level structure associated with topography and land cover. Other studies have found that the MYJ produces a colder (more stable), moister PBL than other schemes (Sun and Barros, 2013; Hu et al., 2010), that local closure schemes such as the MYJ tend to reproduce stable atmospheric conditions better than non-local while the opposite is true for unstable conditions (Shin and Hong, 2011), and that the MYJ performed the best of five PBL schemes in reproducing deep convective cores over India (Madala et al., 2014). These contrasting results from different studies indicate that the choice of PBL scheme depends largely on the characteristics of individual cases and what processes each set of simulations is primarily concerned with studying.

In the inner mountain region, the presence of fog and low level cloud during the July 2012 event was confirmed independently via a webcam located at P3 and maintained by the National Park Service. In order to explore which microphysical parameterization leads to model simulations best able to capture the space–time evolution of low level moisture fields and condensation in the SAM, we ran a sensitivity study for the first ten (after the 6 h of spin-up) hours of the simulation of Case 1 in D03 (the entire simulation was reproduced in D01 and D02). The parameterizations tested consider at least five hydrometeor classes in addition to water vapor in WRF version 3.5.1: Goddard (Tao et al., 1989), Thompson (Thompson et al., 2008), Milbrandt (Milbrandt and Yau, 2005a,b), Morrison (Morrison et al., 2009), WRF Double Moment 6 class (Lim and Hong, 2010) and WRF Single Moment 6 class (Hong and Lim, 2006). Fig. 9 shows mixing ratio profiles for rainwater (QR, dashed lines) and cloudwater (QC, solid lines) below 2 km for selected times along altitudinal gradients in the inner region (P3 and P22) and the open gap (P1 and P8, see Fig. 1 for locations). The actual terrain elevation and the corresponding grid-point elevation in the WRF grid are provided for the locations plotted here in Table 1, organized by location number (Fig. 1). A detailed discussion of each microphysical scheme can be found in the literature cited above. The simulations with the Goddard and Milbrandt schemes were able to consistently exhibit low level clouds and the general observed patterns of cloudiness as well as early morning rainfall (e.g. P22) in the case of Milbrandt. For further guidance, simulated precipitation fields were compared against Stage IV radar-rain gauge estimates (Seo, 1998; comparisons not shown), and finally the Milbrandt scheme was selected for this study as it was determined that using the Goddard microphysics scheme significantly overestimated precipitation for the two events studied here.

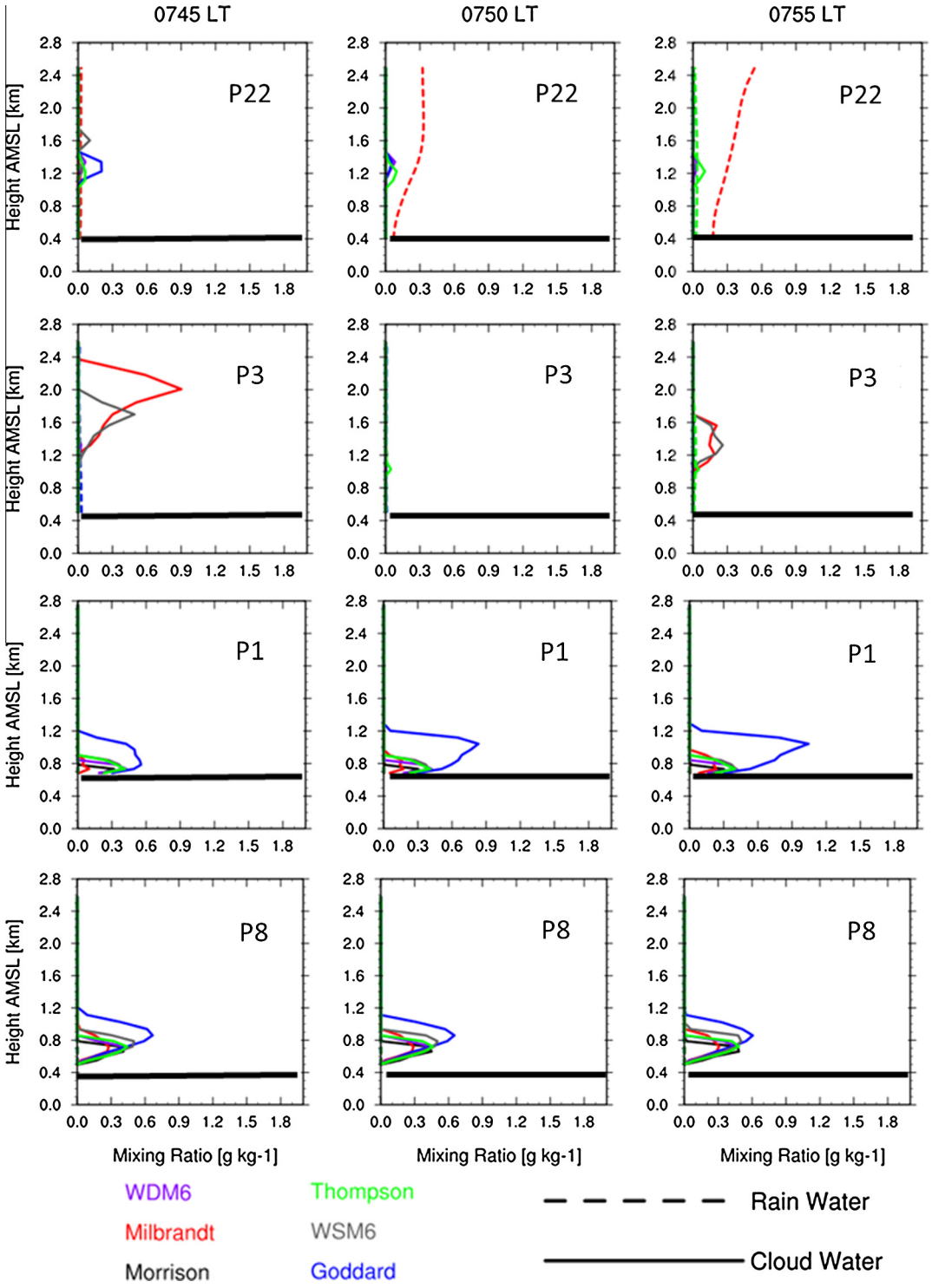


Fig. 9. Hydrometeor profiles simulated with different microphysical schemes for Case 1 are shown here at selected times in the early morning of 9 July 2012 (7:45–7:55 AM local in columns from left to right) along altitudinal gradients in the open gap and in the inner mountain region. The black line in each panel corresponds to that location's elevation as represented by WRF. Rainwater (cloud water) mixing ratios are represented with dashed (solid) lines respectively. Colors correspond to the given microphysical scheme. (For interpretation of the references to color in this figure legend, the reader is referred to the web version of this article.)

4. Modeling results

This section is structured as follows: first, both cases are described in terms of their local observations and overarching synoptic structure. Then, the WRF simulations are examined focusing on low levels wind and moisture convergence patterns. Note that the point is not to provide one more assessment of the model simulations in terms of precipitation timing and amounts in the SAM which has been done (e.g. Sun and Barros, 2012, 2013), but rather to focus on the mechanisms by which low level moisture, a precursor of fog and low level cloud formation, is produced or delivered within the inner mountain region. Details are provided below, but some of the main differences in the two cases are stronger synoptic forcing in Case 2; higher accumulations and intensities in

Table 1
A list of selected locations (see Fig. 1), their geolocation, and actual elevation vs. the grid point representation in WRF.

Location name (map in Fig. 1)	Latitude	Longitude	Actual elevation (m)	Grid point elevation (m)
P1	35.885678	−82.584475	1188	661
P3	35.586100	−83.072530	1493	483
P4	35.562248	−83.497359	1956	377
P8	35.804619	−82.660369	598	478
P21	35.568237	−83.025073	788	516
P22	35.517690	−83.100550	777	384

Case 2; and overnight/early morning timing of storm arrival in Case 2 compared with midday timing in Case 1.

4.1. Case descriptions

(a) Case 1: 9–12 July, 2012: The precipitation event of interest occurred in the early afternoon on 11 July 2012. It was part of a larger, longer-duration precipitation event due to a stationary front in the area, with enhanced convection on 11 July 2012. The observed MRR reflectivity profiles (Fig. 10) show clear differences between the ridge and the valley. A distance of about 12 km separates these sites. At the ridge (P1), consistently high reflectivity values are observed throughout the vertical column. In the valley (P8), the reflectivity gradient is steeper, and much stronger values are observed near the surface. The bright band above the ridge (P1) is slightly stronger than in the valley (P8). Note that the 500 m difference between the bright-band height in the valley and ridge, 3500 m AGL and 3000 m AGL respectively, is due to the difference in topographic elevation (1188 and 598 for P1 and P8 respectively, see Table 1) between the two locations. Event onset in the valley was about 45 min prior to that at the ridge. The highest reflectivity values and rain accumulations in the valley occur around 1400 LT/1800 Z, and at the ridge closer to 1430 LT/1830 Z. At each location, the event was monitored using PARISVEL2s, MRRs, and RGs. The highest intensities were observed in the valley with accumulations that significantly exceeded those at the ridge (by about 30 mm over the ~25 h event period, Fig. 10). There is significant spread among rainfall estimates from various surface instruments (>10 mm over the three hour period simulated with the rainshaft column model in Wilson and Barros, 2014), with the differences persistent throughout the event. The rain gauges, which are susceptible to undercatch, report the highest totals and are shown in Fig. 10.

Previously, the column model simulation of this event was performed for the valley and ridge locations (P8 and P1 respectively, see Fig. 1) in the OG (see Wilson and Barros, 2014 for a detailed description of the column model results). Here, WRF was run for Domain 1 over a 3 day period beginning at July 9 at 0000 Z. Domains 2 and 3 begin on July 9 at 0600 Z, thus allowing a 6 h period for model spin-up.

(b) Case 2: 12–16 May 2014: This case was also associated with a frontal passage; however, this time, a strong cold front passed through the region quickly, and included both convective and stratiform rainfall. This case occurred during the IPHEx IOP (Barros et al., 2014), and thus there is a large amount of ground-

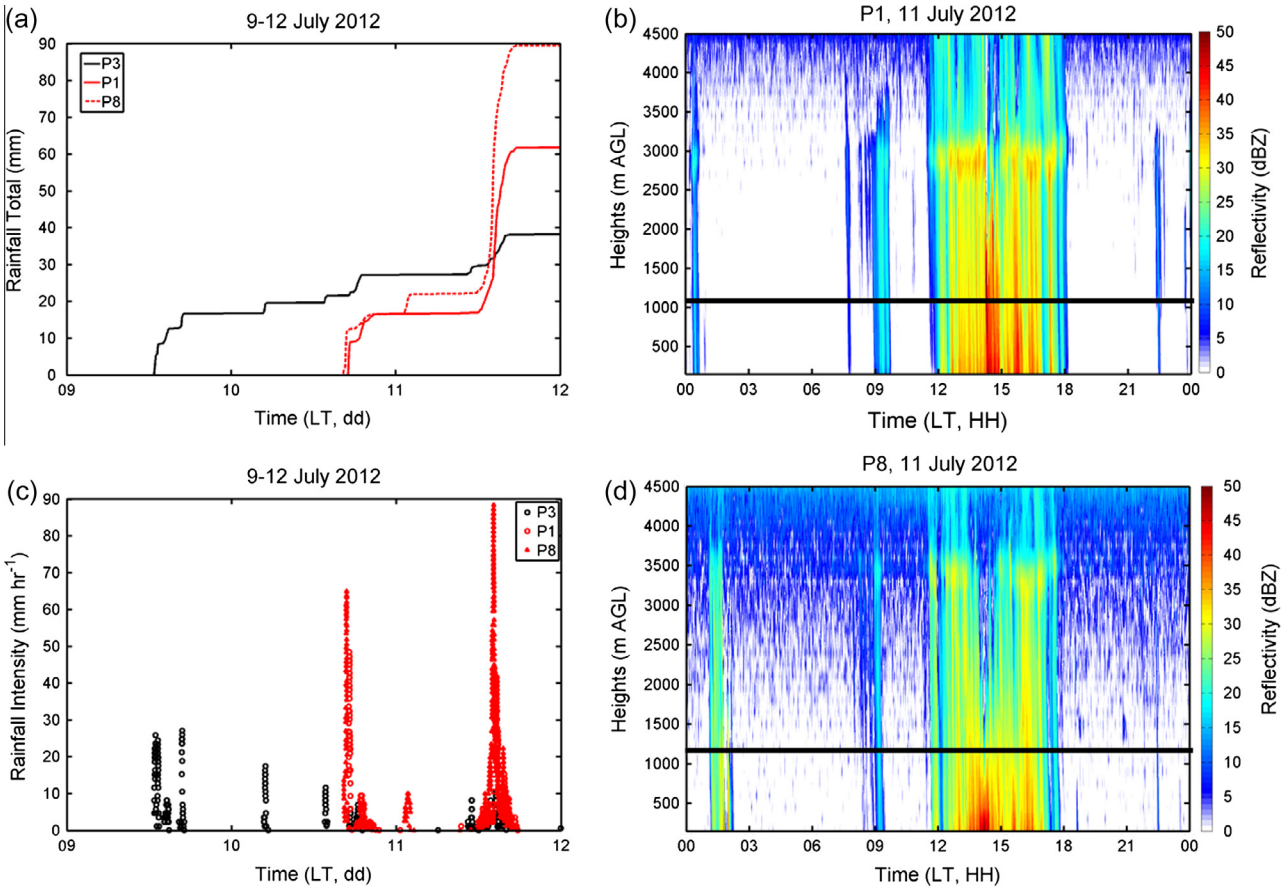


Fig. 10. Case 1 observations from Micro Rain Radars (right) and rain gauges (left) are presented here. Micro Rain Radar observations are shown for the day of most intense precipitation in the open gap region. Rain gauge accumulations are shown for the entire simulation period, for the open gap and the inner mountain region. The black line in the MRR observations represents the level at which observations stop during Case 2 (Fig. 11).

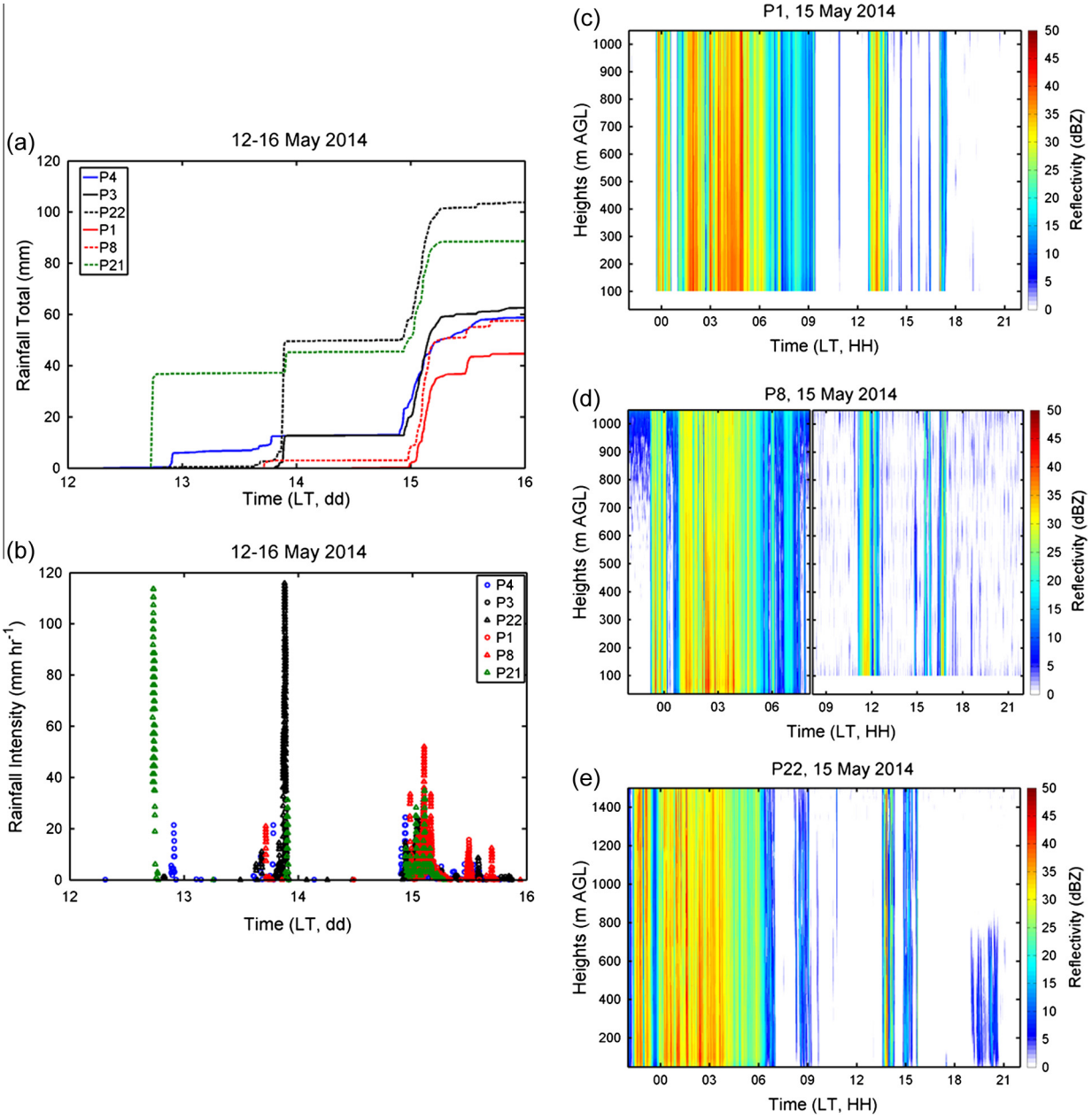


Fig. 11. Case 2 observations from Micro Rain Radars (right) and rain gauges (left) are presented here. Micro Rain Radar observations are shown for the day of most intense precipitation in the open gap region and at P22 (valley in the inner mountain region). Rain gauge accumulations are shown for the entire simulation period, for the open gap, western ridge, and the inner mountain region.

based data available to analyze this event. As the event progressed, the precipitation developed into a squall line. A strong short wave moving out ahead of the main upper level trough caused the precipitation behind the line to move more quickly out of the area than expected considering the slow moving cold front. After the squall line, the regional atmosphere temporarily dried out before scattered low level showers formed on the lee side of the mountains (upper level support remained). The case was simulated in WRF from 0 Z on 12 May (06 Z for D02 and D03) to 0 Z on 16 May. 13 May included diurnal afternoon isolated showers in the mountains. The major difference between Case 2 and Case 1 is that Case 2 was much more strongly synoptically forced, whereas in Case 1 there was a stationary front but the diurnal, localized forcing outweighed the weak synoptic forcing.

As shown in the observations (Fig. 11), in the open gap the strong reflectivity gradient toward the surface in the valley (P8), and stronger convective activity at the ridge (P1) are not present as they were in Case 1. Note that the bright band is not visible at either location due to the finer resolution and consequently reduced profiling depth of the MRR range gates (reflectivity profiles are available up to 1050 m AGL). In the rainfall totals, the strong low level enhancement feature associated with the presence of low level moisture in Case 1 is absent in the open gap region. The rainfall rates at the valley location (P8) are higher than at P1, but the difference is small, and rainfalls totals are much lower than in Case 1. There is no evidence of deep fog in this case in the open gap. However, the situation is different in the inner region. Unfortunately, the MRR at the ridge (P3) was not functioning during this

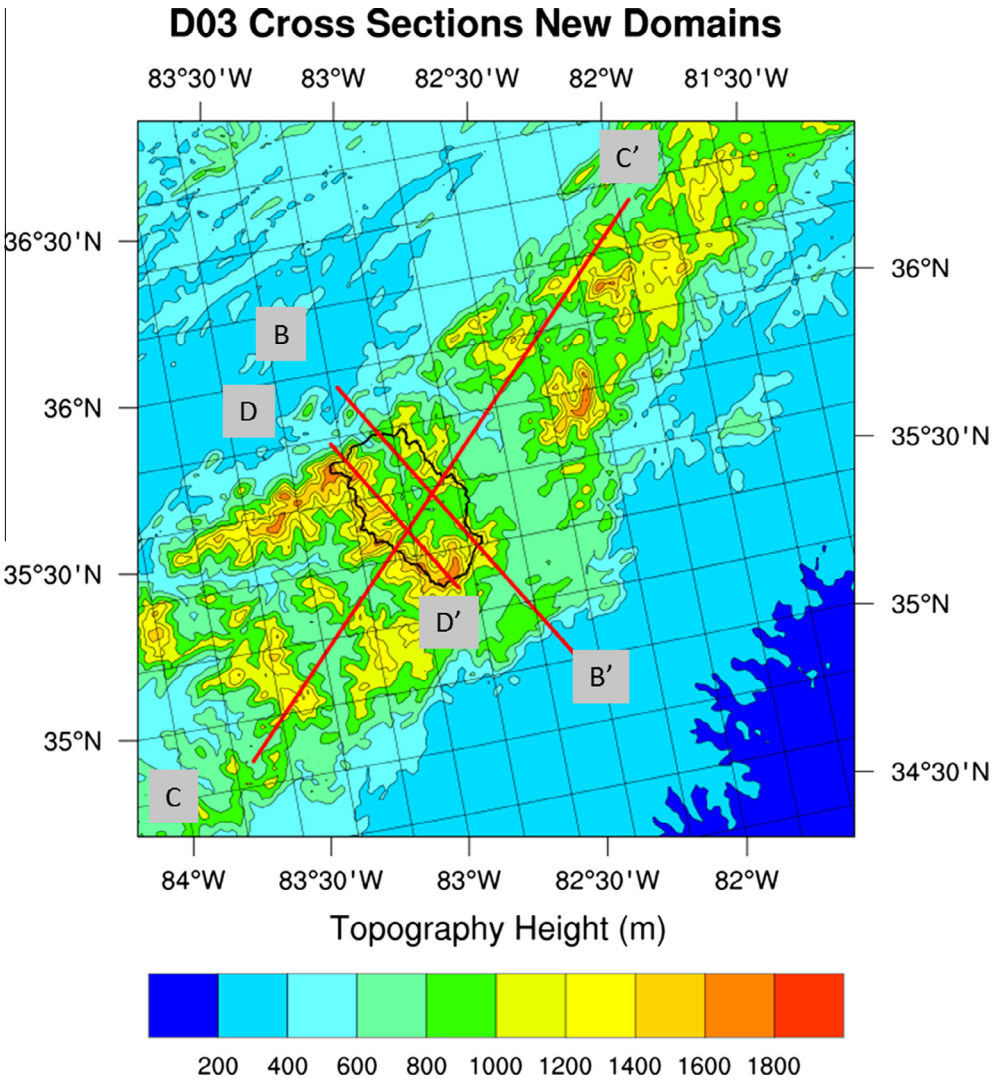


Fig. 12. This figure shows a topographic map of a subset of Domain 3, with cross sections marked that will be used in later figures.

event due to a broken cable. However, the reflectivity profile in the valley (P22) does show the low level enhancement signature similar to the open gap in Case 1. In addition, strong rainfall enhancement is apparent in the inner region (Fig. 11) through the rainfall totals at P21 and P22 (valleys) compared to P3 (ridge).

4.2. Model simulations

In analyzing the WRF simulation output, we will focus on the lowest 500 m above ground level (the lowest 10 levels simulated with the model). Cross sections that will be used throughout the analysis are marked in Fig. 12. B–B′ is a northwest–southeast slice down the valley in the Pigeon River Basin. C–C′ is oriented along the main axis of the SAM (SW–NE) and spans the inner region and the open gap (i.e. P1 and P8). D–D′ cuts northwest to southeast across the ridgelines in the Pigeon River Basin where the long term rain gauge network is located. To assess the output of the simulations, we will first discuss precipitation timing/onset as compared to in situ rain gauges, and then consider the information from WRF regarding the structure of the near surface in terms of moisture and winds.

4.2.1. Precipitation timing/onset

First, rainfall results across D–D′ are presented for Case 1 (July 2012) and Case 2 (May 2014). One of the metrics used to determine how well WRF was able to resolve the simulated events was how the rainfall event progressed across the domain, that is, the March of the storm. To assess this, we present a time (*y*-axis) versus cross section (*x*-axis) plot showing rain accumulations in contours. This is a modified version of a time–longitude plot first described by Hovmöller (1949) and the diagrams will henceforth be referred to as Hovmöller diagrams. Please note that Hovmöller diagrams should be read with time progressing from top to bottom. On the *x*-axis, the cross-section reads left to right (west to east).

In Case 1 (Fig. 13a and b), instead of frontal-associated rain propagating along the cross-section, scattered showers are present throughout the entire area. Precipitation is not widespread across the whole area or consistently moving in one direction. In this case, the model is within the hour of rain gauge initiations at all ridges and thus, comparatively, it does a much better job of matching with observations in terms of precipitation timing. WRF rainfall begins between 1030 and 1330 LT throughout the D–D′ cross-section, and most rain gauges report rain beginning between 1200 and 1300 LT. However, there is no consistent spatial pattern or organization between the terrain features and rainfall. In Fig. 13b, rain gauges across all ridgelines report precipitation at different times within the midday period of initiation.

In contrast, in the strongly synoptically forced Case 2, WRF precipitation onset is delayed (see Fig. 13c), as compared to the observations, by about 4 h. Nevertheless, the temporal and spatial

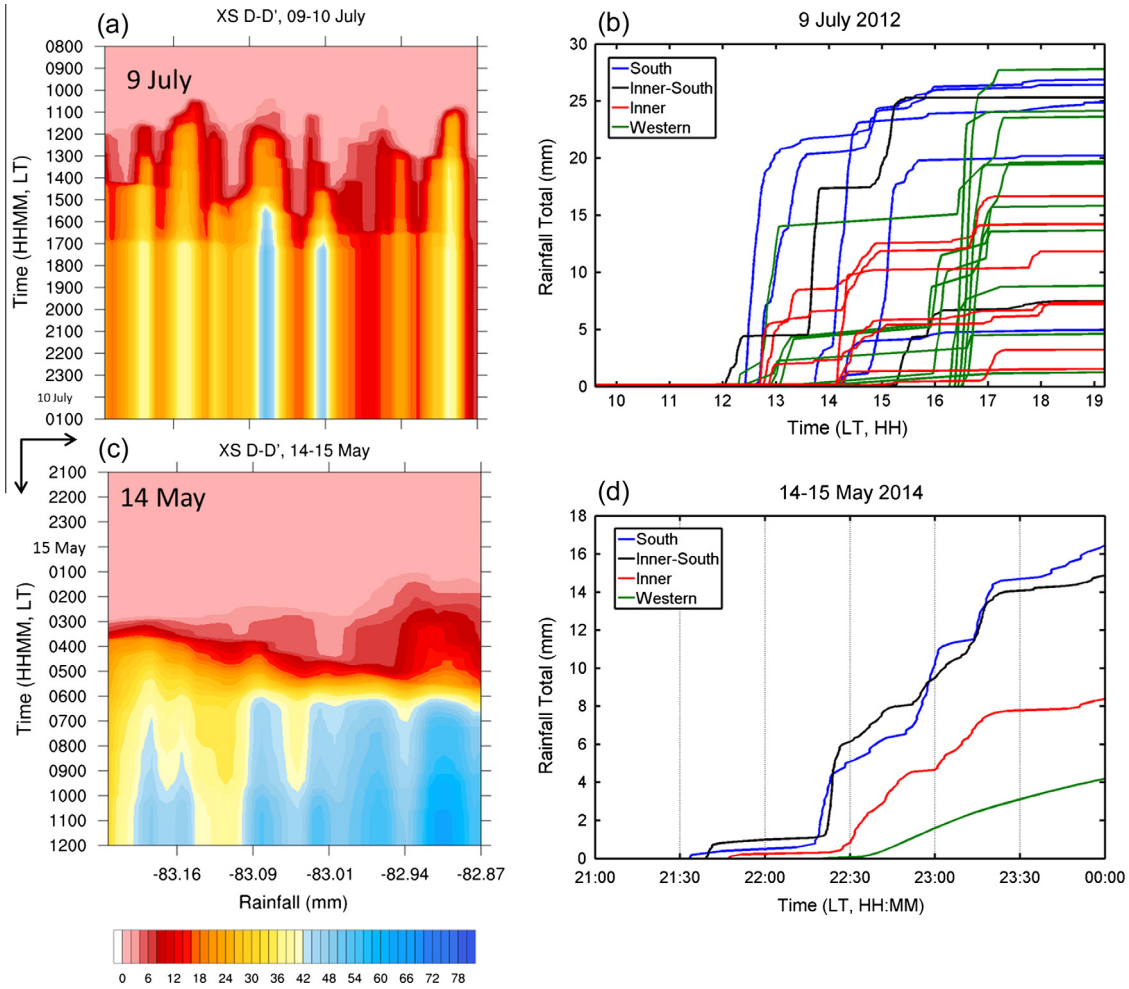


Fig. 13. Rainfall initiation times are shown here for Case 1 (b) and Case 2 (d). For Case 1, all gauges are shown, since there is no neat spatial progression. For Case 2, the first gauge to report in each ridgeline of the Pigeon River Basin is shown. A Hovmöller diagram, for cross section D–D′ (see this figure) of the rainfall reported by WRF at model rainfall initiation time is also shown for Case 1 (a) and Case 2 (c). Note that in Hovmöller diagrams time progresses from top to bottom and longitude progresses from left to right (w–e).

progression across the Pigeon River Basin followed that of the observations (see Fig. 13d). The plots present rain gauge accumulations, with each ridge represented by the first gauge in that region to report rainfall. There was significant variability within the different ridgelines as to precipitation onset; however, the progression clearly began in the southeast gauges and proceeded to the west. WRF captures that variability in good agreement with the observations.

4.2.2. Assessing topographic modulation of low level moisture structure

The contribution of convergence to the moisture availability in the inner SAM can be estimated from the moisture budget, expressed as:

$$\frac{\partial W}{\partial t} = E - \nabla \cdot F_M - R \tag{3}$$

where the left hand side is the change in precipitable water (W) over the column; on the right hand side the first term is the contribution from terrestrial evapotranspiration (E), the second term represents moisture divergence ($\nabla \cdot F_M$, where $F_M = \frac{1}{g}\int_0^{p_x} q v_H dp$, q = the water vapor mixing ratio, v_H = the horizontal wind, and p = pressure) calculated from model output, and the third term is rainfall (R). The vertical integration in the second term is computed based on beta factors, after Trenberth (1991). Fig. 14 shows the contribution of each of the terms in Eq. (3), as a time series averaged over the Pigeon River Basin in the inner mountain region. Results are shown for Case 2 from nighttime through early morning on 12 May and 15 May to contrast the moisture budget evolution for two very different synoptic environments. The integrations of precipitable water and moisture convergence over different heights (whole atmospheric column, under 2 km, and under 500 m) show the relative contribution of the low levels depending on the synoptic environment. The precipitable water tendency and the moisture convergence terms are of the same order of magnitude under dry conditions on 12 May, whereas rainfall is a dominant term on 15 May. However, the vertical structure is very different during the night on 12 May consistent with nocturnal stratification of the atmosphere, which is not present on 15 May due to strong synoptic forcing. Note the increasing contribution of evapotranspiration to the moisture budget after sunrise on May 12th, which is very weak into mid-morning on 15 May after the frontal passage due to the persistence of rainfall.

The results from Domain 3 shown in Figs. 15–18 illustrate how the topography modulates flow and affects the moisture profile of the low levels in the atmosphere. First, in Fig. 15, horizontal winds at the lowest model level (10 m) and the vertical structure of the squared moist Brunt–Väisälä frequency (N_m^2), cloud water, and

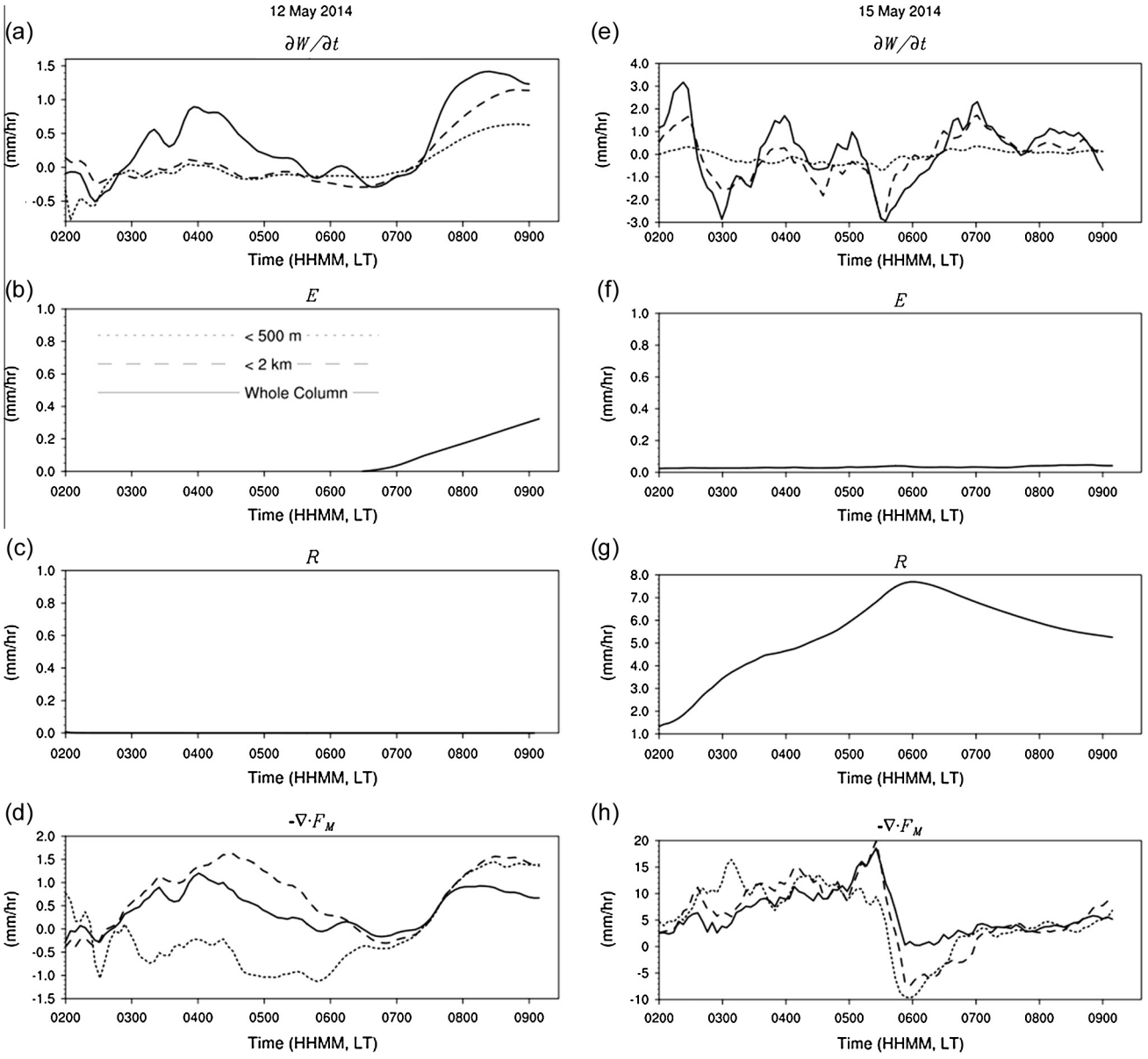


Fig. 14. This figure shows the time series for each term in the moisture budget for (a–d) the morning of 12 May 2014 and (e–h) the morning of 15 May 2014. In plots (a and e) and (d and h) which are for the whole column, solid lines indicate the entire column, dashed lines indicate integration under 2 km, and dotted lines integration under 500 m.

vertical winds along B–B′ at 1200 LT, and the Hovmöller diagram of vertically integrated water vapor in the lower 500 m AGL are presented for each day simulated in 2012 (9/10/11 July across rows a/b/c, respectively). Recall that the terrain representation in WRF is different than that in reality and will cause some discrepancies from the observations for this event. The Brunt–Väisälä frequency is also known as the buoyancy frequency, and is a quantity that is used to assess stability. The purpose of using the moist version of the quantity is to make sure to include the effect of phase changes and latent heating that go along with vertical displacements in a moist atmosphere. It is calculated by:

$$N_m^2 = g\left\{\frac{1+\left(\frac{L_v q_s}{R_d T}\right)}{1+\left(\frac{\varepsilon L_v^2 q_s}{c_p R_d T^2}\right)}\left(\frac{d\ln\theta}{dz}+\frac{L_v}{c_p T}\frac{dq_s}{dz}\right)-\frac{dq_w}{dz}\right\} \quad (4)$$

where g is gravitational acceleration, L_v is the latent heat of vaporization, c_p is the specific humidity at constant pressure, R_d is the gas constant for dry air, q_s is the saturated mixing ratio computed from WRF output of relative humidity and water vapor mixing ratio, q_w is the vapor and liquid mixing ratio (here calculated by combining the mixing ratios for water vapor, cloud water, and rain water), ε is the ratio of the dry air gas constant to the water vapor gas constant, θ is potential temperature, and T is the environmental temperature, z is the height, and N_m^2 has units of s^{-2}. This method for calculating the moist Brunt–Väisälä frequency was derived in Durran and Klemp (1982). In the inner region, the rainfall is higher on 9 July than it is on 11 July (see Fig. 10a and c). Notice the drying of the lower atmosphere in the B–B′ cross section with increased stability and reduced vertical motion as time progresses (central panels). The times plotted in the Hovmöller diagrams are 0600–1400 LT to focus on the early morning to mid-day transition that is important in this case. In each plot, the gradient from southeast to northwest is wetter to drier, and the water vapor content increases at low levels as the day progresses on the 9th and 10th. The time for the horizontal wind field plots in the first column and the vertical cross sections of vertical velocity, cloud water, and N_m^2 in the second column is at

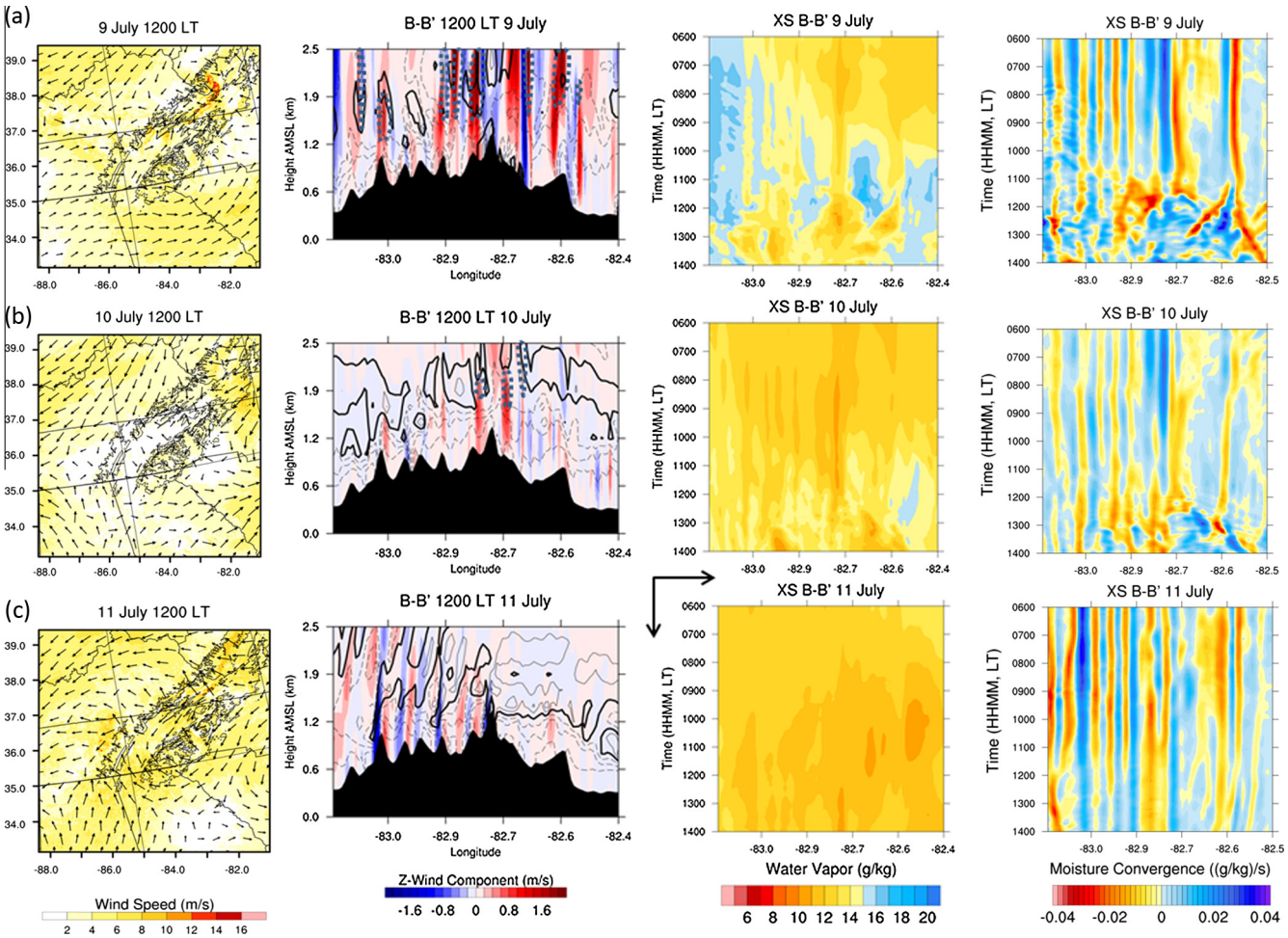


Fig. 15. This figure shows model simulation output for Case 1, with columns from left: horizontal wind fields in Domain 3; B–B′ cross-sections of vertical velocity with squared saturated Brunt–Väisälä frequency contours (with a step of 0.0001 s^{-2}, and the zero contour shown as a thicker line) and outlined hatch marks to represent the presence of cloud water hydrometeors, identified with a threshold of 0.02 g/kg; B–B′ Hovmöller diagrams of vertically integrated water vapor within 500 m above ground level; B–B′ Hovmöller diagrams of vertically integrated moisture convergence within 500 m of ground level. All three days are shown, with cross sections at noon local time and the Hovmöller diagrams from 0600 to 1400 local time. Note that in Hovmöller diagrams time progresses from top to bottom and longitude progresses from left to right (w–e).

noon local time each day. The wind fields begin with predominantly westerly/southwesterly flow entering the region of interest. On 10 July, the wind fields are beginning to transition to those shown on 11 July, where colder and drier air begins to move into the region from the N–NE. Vertical velocity fields in the middle column show couplets with the strongest flow generally on the southeast side of the peaks. The effect of the terrain as a barrier to horizontal surface winds and an obstacle forcing stronger vertical motion is shown in each subplot for this weakly synoptically forced case. Observed patterns on 9 July is associated with the westerly/southwesterly flow locally.

Along the same southeast/northwest cross-section in Case 2 (May 2014), the strong synoptic forcing is illustrated in Fig. 16 through a comparison of the air motion and moisture fields between 12 May, before the cold front entered the region, and 15 May, where 0800 LT is in the midst of the event. The relevant Hovmöller diagram time interval in the May 2014 case is 0200–1000 LT. The squall line passing through the region of interest is easily traced in the wind field plot as well as in the Hovmöller diagrams of low level moisture convergence and water vapor. On 12 May, the moisture convergence patterns are organized and follow the terrain patterns. Note that in general the water vapor concentrations in Case 2 are much lower than during Case 1. The N_m^2 values on the two dates shown here for Case 2 illustrate the presence of two distinctly different regimes between days along the cross section, where on the 12th to the east there is a deep and well mixed layer that becomes increasingly unstable to the west with a large near-surface gradient, although the values are all positive indicating an overall statically stable atmosphere. The pattern on 15 May does not change very much in the lower 2 km but also exhibits a stronger gradient to the northwest, in addition to much stronger vertical velocities. On 15 May, the atmosphere is strongly driven by the overall dynamics of the frontal passage, where on 12 May it is controlled by the thermodynamics (especially note the differences in the concentration of the moist Brunt–Väisälä frequency contours and the strength of the vertical motion between these two dates).

The blocking effect of the terrain is again clear in the surface horizontal wind plots on 12 May, as well as the winds funneling through the inner pass between the French-Broad and the Pigeon River Basins. Southerly low level flow at the beginning of the simulation to the west of the mountains contrasts with quiet conditions on the eastern side of the mountains, and becomes strongly westerly on 15 May. In general, corresponding with the frontal passage, 10 m wind speeds are much higher on the 15th. While in both cases flow and moisture patterns are organized around the terrain during most of the simulation, in Case 2 the disruption associated with the front is significant in all fields shown. This indicates that

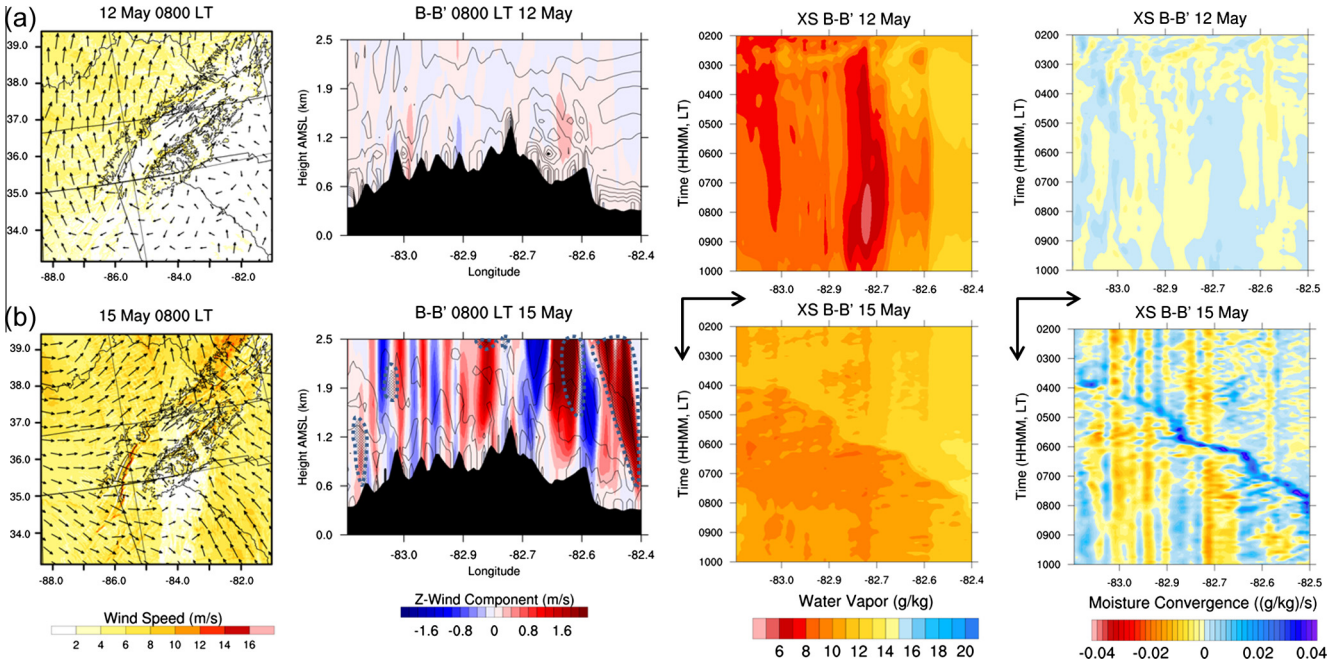


Fig. 16. This figure shows cross sections B–B′ for Case 2, with columns as in Fig. 15: (a) shows 12 May 2014, with cross sections at 0800 local time and Hovmöller diagrams from 0200 to 1000 local time, and (b) 15 May 2014, with the same times of day. Note that in Hovmöller diagrams time progresses from top to bottom and longitude progresses from left to right (w–e).

the synoptic forcing overcomes the local terrain modulation, even as the terrain and antecedent moisture (i.e. on 12–14 May) may play a role also in the reverse orographic enhancement observed by in situ sensors; specifically, where valleys in the inner mountain region report significantly higher accumulations than ridges (Fig. 11a). The difference in accumulations prior to the frontal passage late on 14 May is on the order of 40 mm, or up to 4 times as much precipitation.

Along the C–C′ northeast to southwest cross section that traverses the Pigeon River Basin as well as the open gap region, Fig. 17 shows an increase in the organization of moisture convergence patterns in the open gap (labeled in the red box overlaid on the plots). Even when these patterns are most disrupted on 9 July after 1200 LT in the Hovmöller diagrams of low-level moisture convergence and water vapor, co-organization with the terrain is still apparent. On the 9th, the water vapor concentration shows a peak at midday and a maximum toward the northeastern end of the cross section, while that same section is the driest on 11 July. Similarly to Fig. 16, stability increases as the days pass (as shown by the move to higher N_m^2 values – note the negative contours near some peaks on 9 and 10 July, and the increase in structure (number of contour lines) as the days pass), and the atmosphere becomes drier. Again note that compared to Case 2, the low level vertical structure of the atmosphere is heavily complex and tied to the terrain.

The C–C′ cross sections (Fig. 18) in Case 2 on 12 May show the terrain-following moisture convergence organization that is seen in Case 1. However, as seen in Fig. 16 in the B–B′ cross section, on 15 May those patterns are severely disrupted by the strong squall line passing through from the southwest to the northeast over six hours. The vertical velocity couplets of mountain waves are significantly stronger on 15 May in the morning during the storm, and cloud formation is simulated in the northeast sector of the cross-section. Note the relative uniformity in the N_m^2 values, especially away from the very near surface, throughout both cross sections, as well as the difference in strength of the vertical velocity and moisture convergence values.

In this case, the strength of the squall line passage at most locations, and specifically the open gap, was such that any enhancement provided by low level moisture was not significant as a percentage of the overall rainfall accumulation and intensities. However, as seen in the observations presented in Fig. 12, there was still significant enhancement of rainfall at low elevations in the inner region valley as compared to the adjacent ridge. Nevertheless, in these more strongly forced synoptic events, it is more challenging to see the low level, highly heterogeneous landform effects at the resolution at which the model was run in this case. Higher resolution simulations are needed in order to better resolve the terrain and quantify its effect.

5. Conclusions and discussion

Persistent patterns of moisture convergence at low levels seen in the model simulations for both cases are consistent with low level cloudiness and fog affecting precipitation intensities and accumulations both under weak and strong synoptic forcing conditions, although the model did not always produce the observed low level cloudiness in particular in areas where the terrain complexity was least well represented. The moisture convergence patterns follow the peaks and valleys as represented by WRF terrain, with landform effectively controlling the timing and spatial structure of convergence hot-spots, as seen in the Hovmöller diagrams presented in Figs. 15–18.

The results in the inner mountain region, where the terrain is least well represented by the WRF grid, should be improved with higher resolution simulations both horizontally and vertically. The contrasting behavior of the inner region and open gap between the two case studies suggests that there is a characteristic timescale of persistent organized moisture convergence associated with fog formation that is dependent upon local environmental conditions such as stability and availability of cloud condensation nuclei (CCN). The presence of low cloud and fog was not successfully simulated in all areas, as expected due to both the imperfect terrain representation in particular in the complex inner mountain

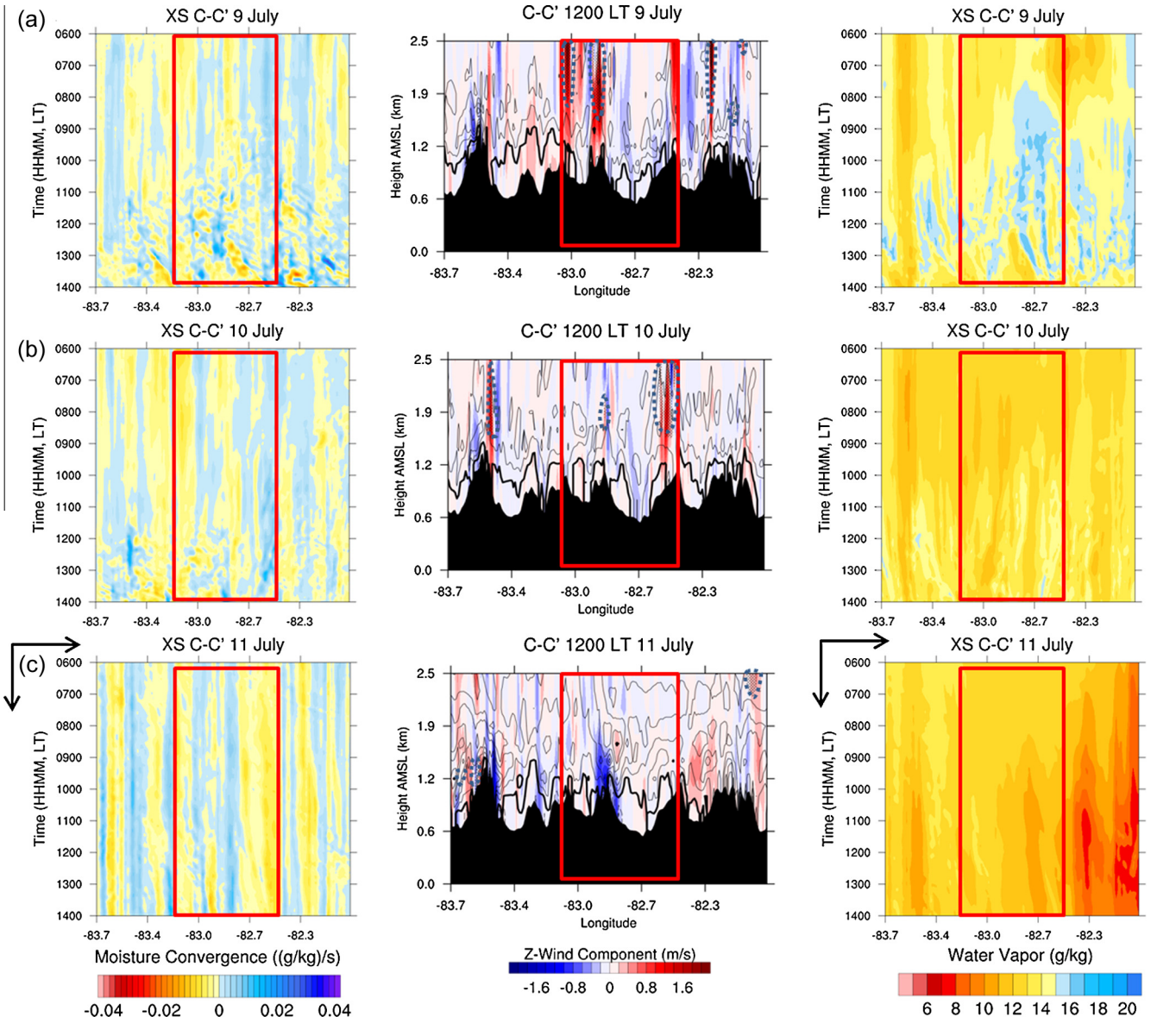


Fig. 17. This figure shows cross sections C–C′ for Case 1, with columns from left: Hovmöller diagrams of vertically integrated moisture convergence under 500 m; cross-sections of vertical velocity with squared saturated Brunt–Väisälä frequency contours (with a step of 0.0001 s^{-2}, and the zero contour shown as a thicker line) and outlined hatch marks to represent the presence of cloud water hydrometeors, identified with a threshold of 0.02 g/kg; Hovmöller diagrams of vertically integrated water vapor under 500 m. (a) shows 9 July, (b) 10 July, and (c) 11 July 2012. Cross sections are at 1200 local time and Hovmöller diagrams go from 0600 to 1400 local time each day. The red box indicates the part of the cross section passing through the inner region (left) and open gap (right side of the box). Note that in Hovmöller diagrams time progresses from top to bottom and longitude progresses from left to right (w–e). (For interpretation of the references to color in this figure legend, the reader is referred to the web version of this article.)

region, as well as the limitations in the model parameterizations to deal with processes occurring at very high resolution; however, moisture build-up that is a necessary precursor takes place at the hypothesized locations. Based on these two case-studies, the inner region more consistently and strongly experiences persistent convergence patterns regardless of the strength of synoptic scale circulations and cyclonic activity, while the open gap is more effectively ventilated during conditions of strong synoptic forcing (note the contrast in updraft strength between the cases). This conclusion is reached because the effect of these low level patterns is apparent in the mountain pass only in the case of weaker synoptic forcing, where in the inner mountain region it is observed in both the weak and strong synoptic cases. The daytime–nighttime import and export of low level moisture may also play a role but is not examined here. Ultimately, this time-scale should be determined by cloud formation processes, including CCN availability and local microphysical processes. Data relevant to address this question were collected during IPHEx, but this is out of the scope of this manuscript. Fundamentally, the simulations support the hypothesized link between altitudinal (ridge–valley) precipitation gradients and horizontal heterogeneity in the vertical structure of low level clouds and precipitation. In particular, the reverse orographic enhancement denoted in the inner nested mountain valleys is formed and strengthened through landform controls on local moisture convergence, where the patterns of low level moisture convergence are shown in Figs. 15–18.

The results from this study also illuminate further questions and suggest other methods with which to extend our investigation and understanding of processes in these and other regions. Ongoing work is focused on improving the terrain representation

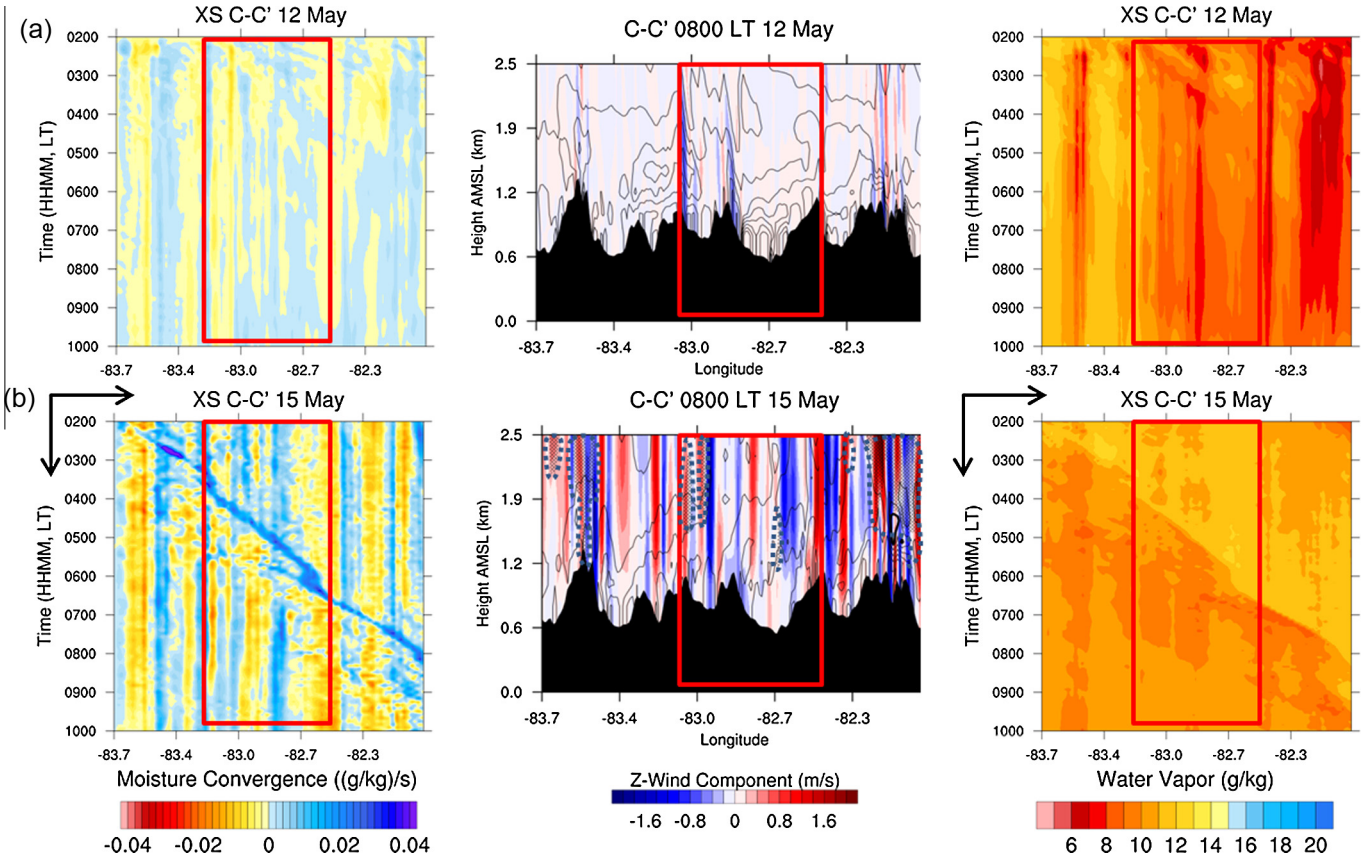


Fig. 18. This figure shows cross sections C–C′ for Case 2, with columns as in Fig. 17: (a) shows 12 May 2014 and (b) 15 May 2014. Cross sections are at 0800 local time and Hovmöller diagrams go from 0200 to 1000 local time each day. The red box indicates the part of the cross section passing through the inner region (left) and open gap (right side of the box). Note that in Hovmöller diagrams time progresses from top to bottom and longitude progresses from left to right (w–e). (For interpretation of the references to color in this figure legend, the reader is referred to the web version of this article.)

in this region, testing using standardized WRF methods and using fractal methods (Bindlish and Barros, 1996) to upscale high resolution terrain data available (30 m) to 1 km resolution. Analysis of all the observational data available from the IPHEx campaign is ongoing as well and expected to result in new insights.

Acknowledgements

The first author acknowledges support by NSF Graduate Research Program Grant 1106401 and the Pratt School of Engineering. The research was funded by NASA Grant NNX13AH39G with the second author. For allowing us to set up instrumentation, we are grateful to Greg Wilson and Pamela McCown, to Asheville-Buncombe Technical Community College, to Paul Super and the National Park Service, and to Neil Carpenter and the Maggie Valley Sanitary District. We thank the University of North Carolina at Asheville and Duke University students who assisted with maintenance and deployment of our RG network and the other instrumentation used in this research. WRF simulations were conducted using computing resources at NCAR (Yellowstone) available through the first author's NSF grant. Xiaoming Sun provided valuable help with initial model set-up. Last, generous support was provided by Florida International University with funds from the National Science Foundation for the first author to present some of this work at the Weather Radar and Hydrology 2014 International Conference.

References

Anderson, E.P., Marengo, J., Villalba, R., Halloy, S., Young, B., Cordero, D., Gast, F., Jaimes, E., Ruiz, D., 2011. Consequences of climate change for ecosystems and ecosystem services in the tropical Andes. In: Herzog, S.K., Martinez, R., Jorgensen, P.M., Tiessen, H. (Eds.), Climate Change and Biodiversity in the Tropical Andes. Inter-American Institute for Global Change Research and Scientific Committee on Problems of the Environment.

Angulo-Martínez, M., Barros, A.P., 2015. Measurement uncertainty in KE-I relationships for soil erosion studies: an evaluation using PARSIVEL disdrometers in the Southern Appalachian Mountains. Geomorphology 228, 28–40.

Barros, A.P., Lettenmaier, D.P., 1994. Dynamic modeling of orographically induced precipitation. Rev. Geophys. 32, 265–284.

Barros, A.P., Petersen, W.A., Schwaller, M., Cifelli, R., Mahoney, K., Peters-Liddard, C., Shepherd, M., Nesbitt, S., Wolff, D., Heymsfield, G., 2014. Integrated Precipitation and Hydrology Experiment 2014 Science Plan. http://dx.doi.org/10.7924/G8CC0XMR.

Bergeron, T., 1950. Über den mechanismus der ausgiebigen niederschläge (On the mechanism of abundant precipitation). In: Berichte des Duetschen Wetterdienstes in der US-Zone, 12, pp. 225–232.

Bergeron, T., 1965. On the low-level redistribution of atmospheric water caused by orography. In: Supp. Proc. Int. Conf. Cloud Phys., Tokyo, May 1965, pp. 96–100.

Bergeron, T., 1968. Studies of the Orogenic Effect on the Areal Fine Structure of Rainfall Distribution. Rep. 6. Meteorological Institute, Uppsala University, Uppsala, Sweden, 42 pp.

Berry, Z.C., Hughes, N.M., Smith, W.K., 2014. Cloud immersion: an important water source for spruce and fir saplings in the Southern Appalachian mountains. Oecologia 174, 319–326.

Bindlish, R., Barros, A.P., 1996. Aggregation of digital terrain data using a modified fractal interpolation scheme. Comput. Geosci. 22, 907–917.

Computational and Information Systems Laboratory, 2012. Yellowstone: IBM iDataPlex System (NCAR Community Computing). National Center for Atmospheric Research, Boulder, CO. <http://n2t.net/ark:/85065/d7wd3xhc>.

Culatta, K.E., Horton, J.L., 2014. Physiological response of Southern Appalachian high-elevation rock outcrop herbs to reduced cloud immersion. Castanea 79 (3), 182–194.

Cunningham, R.M., 1951. Some observations of natural precipitation processes. Bull. Am. Meteorol. Soc. 32, 334–343.

Dudhia, J., 1989. Numerical study of convection observed during the Winter Monsoon Experiment using a mesoscale two-dimensional model. J. Atmos. Sci. 46, 3077–3107.

Durran, D.R., Klemp, J.B., 1982. On the effects of moisture on the Brunt Väisälä frequency. J. Atmos. Sci. 39, 2152–2158.

Erlingis, J.M., Barros, A.P., 2014. A study of the role of daytime land–atmosphere interactions on nocturnal convective activity in the Southern Great Plains during CLASIC. J. Hydrometeorol. 15, 1932–1953.
Foster, P., 2001. The potential negative impacts of global climate change on tropical montane cloud forests. Earth Sci. Rev. 55, 73–106.
Hanna, S.R., Yang, R., 2001. Evaluations of mesoscale models' simulations of near-surface winds, temperature gradients, and mixing depths. J. Appl. Meteorol. 40, 1095–1104.
Hong, S.-Y., Lim, J.-O.J., 2006. The WRF single-moment 6-class microphysics scheme (WSM6). J. Kor. Meteorol. Soc. 42, 129–151.
Hovmöller, E., 1949. The trough-and-ridge diagram. Tellus 1, 62–66.
Hu, H., Zhang, Q., Xie, B., Ying, Y., Zhang, J., 2014. Predictability of an advection fog event over North China. Part I: sensitivity to initial condition differences. Mon. Weather Rev. 142, 1803–1822.
Hu, X.-M., Nielsen-Gammon, J.W., Zhang, F., 2010. Evaluation of three planetary boundary layer schemes in the WRF model. J. Appl. Meteorol. Climatol. 49, 1831–1844.
Janjic, Z.I., 1994. The step-mountain eta coordinate model: further developments of the convection, viscous sublayer, and turbulence closure schemes. Mon. Weather Rev. 122, 927–945.
Jiménez, P.A., Dudhia, J., 2012. Improving the representation of resolved and unresolved topographic effects on surface wind in the WRF model. J. Appl. Meteorol. Climatol. 51, 300–316.
Juvik, J.O., Nullet, D., 1995. Comments on "A proposed standard fog collector for use in high elevation regions". J. Appl. Meteorol. 34, 2108–2110.
Kain, J.S., 2004. The Kain–Fritsch convective parameterization: an update. J. Appl. Meteorol. 43, 170–181.
Kalnay, E., Kanamitsu, M., Kistler, R., Collins, W., Deaven, D., Gandin, L., Iredell, M., Saha, S., White, G., Woollen, J., Zhu, Y., Leetmaa, A., Reynolds, R., Chelliah, M., Ebisuzaki, W., Higgins, W., Janowiak, J., Mo, K.C., Ropelewski, C., Wang, J., Jenne, R., Joseph, D., 1996. The NCEP/NCAR 40-year reanalysis project. Bull. Am. Meteorol. Soc. 77, 437–471.
Kunz, M., 2011. Characteristics of large-scale orographic precipitation in a linear perspective. J. Hydrometeorol. 12, 27–44.
Lim, K.-S.S., Hong, S.-Y., 2010. Development of an effective double-moment cloud microphysics scheme with prognostic cloud condensation nuclei (CCN) for weather and climate models. Mon. Weather Rev. 138, 1587–1612.
Madala, S., Satyanarayana, A.N.V., Narayana Rao, T., 2014. Performance evaluation of PBL and cumulus parameterization schemes of WRF ARW model in simulating severe thunderstorm events over Gadanki MST radar facility – case study. Atmos. Res. 139, 1–17.
Mass, C.F., Ovens, D., Westrick, K., Colle, B.A., 2002. Does increasing horizontal resolution produce more skillful forecasts? Bull. Am. Meteorol. Soc. 83, 407–430.
Mekonnen, G.B., Matula, S., Doležal, F., Fišák, J., 2014. Adjustment to rainfall measurement undercatch with a tipping-bucket rain gauge using ground-level manual gauges. Meteorol. Atmos. Phys. http://dx.doi.org/10.1007/s00703-014-0355-z.
METEK, 2012. MRR Physical Basics, Version 5.2.0.9. Meteorologische Messtechnik GmbH Rep., 20 pp.
Milbrandt, J.A., Yau, M.K., 2005a. A multimoment bulk microphysics parameterization. Part I: analysis of the role of the spectral shape parameter. J. Atmos. Sci. 62, 3051–3064.
Milbrandt, J.A., Yau, M.K., 2005b. A multimoment bulk microphysics parameterization. Part II: a proposed three-moment closure and scheme description. J. Atmos. Sci. 62, 3065–3081.
Mlawer, E.J., Taubman, S.J., Brown, P.D., Iacono, M.J., Clough, S.A., 1997. Radiative transfer for inhomogeneous atmospheres: RRTM, a validated correlated-k model for the longwave. J. Geophys. Res. 102, 16663–16682.
Morrison, H., Thompson, G., Tatarskii, V., 2009. Impact of cloud microphysics on the development of trailing stratiform precipitation in a simulated squall line: comparison of one- and two-moment schemes. Mon. Weather Rev. 137, 991–1007.
National Centers for Environmental Prediction/National Weather Service/NOAA/U.S. Department of Commerce, 2000. NCEP FNL Operational Model Global Tropospheric Analyses, Continuing from July 1999. Research Data Archive at the National Center for Atmospheric Research, Computational and Information Systems Laboratory, Boulder, CO. http://dx.doi.org/10.5065/D6M043C6 (available online at 2014) (accessed 3 October).
Pounds, A., Fogden, M.P.L., Campbell, J.H., 1999. Biological response to climate change on a tropical mountain. Nature 398, 611–615.
Prat, O.P., Barros, A.P., 2007. A robust numerical solution of the stochastic collection-breakup equation for warm rain. J. Appl. Meteorol. Climatol. 46, 1480–1497.
Prat, O.P., Barros, A.P., 2010. Ground observations to characterize the spatial gradients and vertical structure of orographic precipitation – experiments in the inner region of the Great Smoky Mountains. J. Hydrol. 391, 141–156.
Richardson, A.D., Denny, E.G., Siccama, T.G., Lee, X., 2003. Evidence for a rising cloud ceiling in eastern North America. J. Clim. 16, 2093–2098.
Seo, D.J., 1998. Real-time estimation of rainfall fields using radar rainfall and raingauge data. J. Hydrol. 209, 131–147.
Sevruk, B., Nespor, V., 1998. Empirical and theoretical assessment of the wind induced error of rain measurement. Water Sci. Technol. 37, 171–178.
Shin, H.H., Hong, S.-Y., 2011. Intercomparison of planetary boundary-layer parameterizations in the WRF model for a single day from CASES-99. Bound. Layer Meteorol. 139, 261–281.
Skamarock, W.C., Klemp, J.B., Dudhia, J., Gill, D.O., Barker, D.M., Duda, M.G., Huang, X., Wang, W., Powers, J.G., 2008. A Description of the Advanced Research WRF Version 3. Report TN475+STR. NCAR, Boulder, CO.
Smith, R.B., Schafer, P., Kirshbaum, D.J., Regina, E., 2009. Orographic precipitation in the tropics: experiments in Dominica. J. Atmos. Sci. 66, 1698–1716.
Sun, B., Karl, T.R., Seidel, D.J., 2007. Changes in cloud-ceiling heights and frequencies over the United States since the early 1950s. J. Clim. 20, 3956–3970.
Sun, Xiaoming, Barros, A.P., 2012. The impact of forcing datasets on the high-resolution simulation of tropical storm Ivan (2004) in the Southern Appalachians. Mon. Weather Rev. 140, 3300–3326.
Sun, X., Barros, A.P., 2013. High resolution simulation of Tropical Storm Ivan (2004) in the Southern Appalachians: role of planetary boundary layer schemes and cumulus parameterization. Quart. J. R. Meteorol. Soc. 140, 1847–1865.
Sun, X., Barros, A.P., 2015. Isolating the role of surface evapotranspiration on moist convection along the eastern flanks of the tropical Andes using a quasi-idealized approach. J. Atmos. Sci. 72, 243–261.
Tao, Jing., Barros, A.P., 2014. Coupled prediction of flood response and debris flow initiation during warm- and cold-season events in the Southern Appalachians, USA. Hydrol. Earth Syst. Sci. 18, 367–388.
Tao, Jing, Barros, A.P., 2013. Prospects for flash flood forecasting in mountainous regions – an investigation of Tropical Storm Fay in the Southern Appalachians. J. Hydrol. 506, 69–89.
Tao, W.-K., Simpson, J., McCumber, M., 1989. An ice–water saturation adjustment. Mon. Weather Rev. 117, 231–235.
Terando, A.J., Costanza, J., Belyea, C., Dunn, R.R., McKerrow, A., Collazo, J.A., 2014. The southern megalopolis: using the past to predict the future of urban sprawl in the Southeast U.S. PLoS ONE 9 (7), e102261.
Tewari, M., Chen, F., Wang, W., Dudhia, J., LeMone, M.A., Mitchell, K., Ek, M., Gayno, G., Wegiel, J., Cuenca, R.H., 2004. Implementation and verification of the unified NOAH land surface model in the WRF model. In: 20th Conference on Weather Analysis and Forecasting/16th Conf on Numerical Weather Prediction, pp. 11–15.
Thompson, G., Field, P.R., Rasmussen, R.M., Hall, W.D., 2008. Explicit forecasts of winter precipitation using an improved bulk microphysics scheme. Part II: implementation of a new snow parameterization. Mon. Weather Rev. 136, 5095–5115.
Tokay, A., Wolff, D.B., Petersen, W.A., 2014. Evaluation of the new version of the laser-optical disdrometer, OTT PARSIVEL2. J. Atmos. Ocean. Technol. 31, 1276–1288.
Trenberth, K., 1991. Climate diagnostics from global analyses: conservation of mass in ECMWF analyses. J. Clim. 4, 707–722.
U.S. Census Briefs, 2011. Population Distribution and Change: 2000 to 2010. Prepared by Mackun, P., and S. Wilson. U.S. Department of Commerce, Economics and Statistics Administration.
van der Velde, I.R., Steeneveld, G.J., Wichers Schreur, B.G.J., Holtslag, A.A.M., 2010. Modeling and forecasting the onset and duration of severe radiation fog under frost conditions. Mon. Weather Rev. 138, 4237–4253.
Viale, M., Houze Jr., R.J., Rasmussen, K.L., 2013. Upstream orographic enhancement of a narrow cold-frontal rainband approaching the Andes. Mon. Weather Rev. 141, 1708–1730.
Williams, A.P., Schwartz, R.E., Iacobellis, S., Seager, R., Cook, B.I., Still, C.J., Husak, G., Michaelsen, J., 2015. Urbanization causes increased cloud base height and decreased fog in coastal Southern California. Geophys. Res. Lett. 42, 1527–1536.
Williams, C.R., Bringi, V.N., Carey, L.D., Chandrasekar, V., Gatlin, P.N., Haddad, Z.S., Meneghini, R., Munchak, S.J., Nesbitt, S.W., Petersen, W.A., Tanelli, S., Tokay, A., Wilson, A., Wolff, D.B., 2014. Describing the shape of raindrop size distributions using uncorrelated mass spectrum parameters. J. Appl. Meteorol. Climatol. 53, 1282–1296.
Wilson, A.M., Barros, A.P., 2014. An investigation of warm rainfall microphysics in the Southern Appalachians: orographic enhancement via low-level seeder-feeder interactions. J. Atmos. Sci. 71, 1783–1805.
Wooten, R.M., Gillon, K.A., Witt, A.C., Latham, R.S., Douglas, T.J., Bauer, J.B., Fuemmeler, S.J., Lee, L.G., 2008. Geologic, geomorphic, and meteorological aspects of debris flows triggered by Hurricanes Frances and Ivan during September 2004 in the Southern Appalachian Mountains of Macon County, North Carolina (southeastern USA). Landslides 5, 31–44.
Yuter, S.E., Houze Jr., R.A., 1995. Three-dimensional kinematic and microphysical evolution of Florida cumulonimbus. Part II: frequency distributions of vertical velocity, reflectivity, and differential reflectivity. Mon. Weather Rev. 123, 1941–1963.
Yuter, S.E., Stark, D.A., Crouch, J.A., Payne, M.J., Colle, B.A., 2011. The impact of varying environmental conditions on the spatial and temporal patterns of orographic precipitation over the Pacific Northwest near Portland, Oregon. J. Hydrometeorol. 12, 329–351.
Zhang, H., Pu, Z., Zhang, X., 2013. Examination of errors in near-surface temperature and wind from WRF numerical simulations in regions of complex terrain. Weather Forecast. 28, 893–914.